UNIVERSITY OF ZULULAND

Gas Sensing Properties of Doped Copper Oxide (CuO) Thin Films and Nanostructures

A Dissertation presented to the Department of Physics and Engineering of the Faculty of Science and Agriculture

By

Ms. Ongezwa Mnethu

In Partial-fulfillment of the Requirements for the Master's Degree in Physics at the University of Zululand

Supervisor: Dr. S.S. Nkosi

Co-Supervisor: Dr. C.L. Ndlangamandla

2021

Declaration

I, the undersigned, hereby declare that the work contained in this thesis is my own original work and that I have not previously in its entirety or in part submitted it at any university for a degree.

Signature: ……. 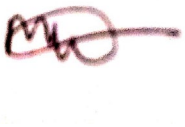

Date: **01 SEPTEMBER 2021**……

LIST OF ABBREVIATIONS

1. CuO - Copper Oxide
2. Zn - Zinc
3. PL - photoluminescence
4. WHO -World Health Organization
5. UN -United Nations
6. VOCs -Volatile organic compounds
7. OSHA - Occupational Safety and Health Administration
8. CDC- Centre for Disease Control
9. SMOs - Semiconducting metal oxides
10. $NiMoO_4$ - Nickel(II) Orthomolybdate
11. NiO - Nickel (II) oxide
12. Co_3O_4 - Cobalt(II,III) oxide
13. WO_3 -Tungsten oxide
14. Cr-Chromium
15. Ni -Nickel
16. ZnO - Zinc oxide
17. $NiCo_2O_4$ - Nickel colbatite
18. Fe_2O_3 -Iron(II,III) oxide
19. BXT - benzene, xylene and toluene
20. SEM - Scanning Electron Microscopy
21. XRD - X-Ray Diffraction
22. UV Vis - Ultra Violet Visible Spectroscopy
23. VSM - Vibrating Sample Magnetometer
24. XPS - X-ray Photoelectron Spectroscopy
25. SnO_2 - Tin dioxide
26. Pt - Platinum
27. Ru -Ruthenium
28. Pd -Palladium
29. NO_2 -Nitrogen dioxide
30. NO - Nitrogen oxide
31. CO_2 - Carbon dioxide
32. CO -Carbon monoxide
33. PSD - position sensitive detector
34. FWHM -full-width-half-maximum
35. EDS -Energy Dispersed Spectroscopy
36. TEM - transmission electron microscope
37. VSM -Vibrating Sample Magnetometer
38. MnO - Manganese (II) oxide
39. CoO-Cobalt(II) oxide
40. LIBs - lithium-ion batteries
41. EMs -energetic materials
42. Cao- Calcium oxide
43. NaOH - sodium hydroxide
44. HR-TEM -High-resolution transmission electron microscope

45. BET - Brunauer-Emmett-Teller (BET)
46. (W-H) -William-Hall
47. $Cu(OH)_2$-Copper(II) hydroxide
48. SAED - selected area electron diffraction
49. LPG - liquefied petroleum gas
50. ESI
51. $ZnFe_2O_4$ -Zinc Ferrite
52. PL -Photoluminescence
53. N_2-Dinitrogen
54. PM - paramagnetic
55. Co- Cobalt
56. Sn-Tin
57. TiO_2- Titanium dioxide
58. $NiWO_4$- Nickel tungstate
59. Zinc nitrate hexahydrate-$Zn(NO_2)_3 \cdot 6H_2O$

Abstract

p-xylene is a harmful volatile organic compound that needs to be tested for indoor air quality detection. We report on the sensing characteristics of CuO and Zn doped CuO nanoplatelets of various concentrations that were prepared by hydrothermal synthesis, against nine different gases. These CuO and Zn based nanoplatelets were characterized by X-ray diffraction, X-ray photoelectron spectroscopy, photoluminescence emission and vibrating sample magnetometer measurements. CuO and 0.1 at. % Zn doped CuO samples were most sensitive and selective to p-xylene gas with relatively high responses (R_a/R_g ratio) of about 42 and 53 at an operating temperature of 150 °C, respectively. These responses were about six times higher compared to the other 8 tested interfering gases. All these samples further exhibited a paramagnetic behavior at room temperature, due to small traces of point defects, such as oxygen vacancies. Both these sensor materials did not show green luminescence at room temperature that is normally associated with oxygen vacancies. However, temperature dependent photoluminescence (PL) measurements for the 0.1 at. % Zn doped CuO showed broad visible emission, including green luminescence, which increased with temperature up to 150 °C and coincided with the gas sensing temperature. The pure CuO, however, showed a rapid quenching in PL emission with an increase in the temperature up to 150 °C. Nevertheless, both pure CuO and 0.1 at. % Zn doped CuO based sensors were highly sensitive to the p-xylene gas. The mechanism associated to the xylene superior sensing was considered in terms of point defects and surface area as active sites for adsorption of gas molecules.

Keywords: CuO, Gas sensor, Thin films and nanostructures, Gas sensing properties.

Acknowledgements

I would like to extend my gratitude and sincere appreciation to the following group of people, without whose assistance and encouragement this work would not have been possible.

- God who have kept me alive, giving me strength and courage through all difficulties and challenges.
- The *Late* Prof. O.M Ndwandwe, Executive Director, Zululand University, for his guidance and encouragement throughout his supervision of this work.
- The Drs. S.S. Nkosi and CL Ndlangamandla, Lecturers at the University of Zululand, Department of Physics, for helping me in operating the gas sensor and providing guidance throughout the supervision of this work.
- Prof. D.E. Motaung, Materials Research Scientist, CSIR, for his advices (academic) and input in this work.
- Mr. A.P. Sefage, a former lab. assistance at University of Zululand, for his assistance in analyzing X-Ray Diffraction results.
- Dr. Ioannis Kortidis for his good assistance during the time for gas sensing.
- Mr. C.T. Thethwayo, a Research Scientist, Zululand University for sharing with me his knowledge of Scanning Electron Microscopy.
- Prof. Eric Njoroge, Material Research Scientist, University of Pretoria for sharing with me his knowledge of Rutherford Backscattering Spectroscopy.
- My mother, father and husband for their support and understanding throughout the time I was away.

- All my friends in and out of the academic field for their support and help.
- National research foundation (NRF) for financial support.
- University of Zululand Research office particularly Ms. Daniela Viljoen.

Publication

- **Ongezwa Mnethu**, Steven S. Nkosi*, Ioannis Kortidis, David E. Motaung, R.E. Kroon, Hendrik C. Swart, Napo G. Ntsasa, James Tshilongo, Thomas Moyo. ***Ultra-Sensitive and Selective p-xylene Gas Sensor at Low Operating Temperature Utilizing Zn doped CuO Nanoplatelets: Insignificant Vestiges of Oxygen Vacancies***. Journal of Colloids and Interface Science 576 (2020) 364 – 375. **IF 8.128**

TABLE OF CONTENTS

LIST OF FIGURES

LIST OF TABLES

CHAPTER I

1.1. Introduction

The World Health Organization (WHO) estimated that over 12 million people had died as a result of unhealthy living and working conditions and poor air quality. Since then, the WHO has been monitoring the quality of air indoor environments. In 2018, WHO held its first global conference in collaboration with the United Nations (UN) Environment on indoors and outdoors air quality in Geneva in order to minimize deaths. Volatile organic compounds (VOCs) and other gases (e.g. xylene, toluene, benzene, ethanol, propanol, ammonia, ethylene, hydrogen, and liquefied petroleum gas) exist in our living and working environments and are well known as harmful gases that attack the nervous system **[1-8]**.

The Occupational Safety and Health Administration (OSHA) has recommended a long-time permissible exposure limit of 100 parts per million (ppm) of xylene [8]. According to the Centre for Disease Control and prevention (CDC), a short-time exposure to as low as 50 ppm may cause skin and eye irritation, impairment to the respiratory system, headache, and dizziness [8]. This therefore suggests the critical importance of xylene detection to environmental safety. Semiconducting metal oxides (SMOs) are known to be suitable gas sensing materials to detect and monitor indoor environments **[1-9]**. The development of such SMO sensing devices that are suitable for the detection of xylene

gas is limited due to the fact that they only operate at higher temperatures that result in higher power consumption and poor selectivity and long-term stability.

There have been many attempts to fabricate gas sensors for xylene detection **[1-16]**. These reports demonstrate mixed combinations of metal oxide and heterojunctions and homojunctions of n-p, p-n and p-p types as the basis of functional materials for xylene gas sensors including $NiO/NiMoO_4$ **[1]**, W doped NiO **[2]**, 4 at. % $Cr:WO_3$ **[3]**, Co_3O_4 **[4]**, 0.3 at. % Au doped WO_3 **[5]**, 3 at. % Sn:NiO **[6]**, 1.5 at. % Sn:NiO **[7]**, Cr:NiO **[9]**, Co doped ZnO **[10]**, Ni doped ZnO **[11]**, $NiCo_2O_4$ decorated on top of WO_3 nanofibers **[12]**, ZnO **[13]**, α-Fe_2O_3 **[14]**, 3D flower- and 2D sheet-like CuO nanostructures **[15]** and WO_3 decorated anatase TiO_2 **[16]**. Most of these sensors for xylene detection contain Ni and/or NiO as a main host or dopant, due to its high thermal stability and high level of oxygen adsorption. The investigations of xylene performances based on SMOs date back about a decade. Little information about copper oxide (CuO) or Zn doped CuO for VOC detection has been reported, especially on the xylene gas selectivity sensing performance.

Copper oxide (CuO) is a p-type semiconducting transition metal oxide with a monoclinic crystal structure, having a relatively small band gap of 1.2 eV **[17, 18]**. It is a novel material that is easily available, with a low processing costs and is non-toxic in nature. It also has excellent thermal stability, good optical and electrical properties. Hence, the unique physical, chemical and electrical properties of CuO have many potential applications in the fields of photocatalysts **[19]**, batteries **[20]**, gas sensor **[15]**, solar cells **[21]** and biosensors **[22]**.

The doping in all these cases is mainly to modify the optical and electrical properties of CuO by addition of foreign impurity ions into its lattice. Amongst all these transition metal dopants mentioned elsewhere [17, 23], Zn^{2+} cations have been found to be in dopant because of their similar ionic radii, i.e. Zn^{2+} (0.60 Å) and Cu^{2+} (0.57 Å). Hence, Zn^{2+} can easily be incorporated into the CuO lattice without distorting the crystal structure or significantly altering the grain size **[24]**. There are a variety of reports based on p-xylene gas selectivity and sensitivity, which are really based on the sensor surface morphology. High responsiveness attributed to the oxygen vacancies and nano-scaling in the SMOs has been reported in the literature **[1, 4, 10, 11, 25, 26]**. Woo *et al*. **[11]** reported a response of 42.44 at 400 °C from Ni doped ZnO nanowire networks and 19.55 **[10]** from nanowire networks of Co-doped ZnO. The highest p-xylene gas response (S = 343.5 at 350 °C) was reported from NiO/$NiWO_4$ yolk-shell spheres **[1]**. The rose-like Co_3O_4 structures recorded as high as 79.8 at 150 °C against 100 ppm of p-xylene **[4]**. The porous coral-like $NiCo_2O_4$ nano-spheres recorded a response of 16.4 at 260 °C and oxygen vacancy dominated CuO@$ZnFe_2O_4$ yolk-shell microspheres recorded 24.1 at 225 °C **[25, 26]**.

In all these reports, a relatively low p-xylene gas response was recorded and these sensors operate at relatively high temperatures above 150 °C. The report by Yang *et al*. **[15]** on CuO nano-flower and nano-sheet structures for xylene gas sensing only demonstrated a low response of 3.5 at a very high concentration of 500 ppm of xylene and at relatively high operating temperature of 260 °C.

Furthermore, it is known to be challenging for SMO sensors to detect benzene, xylene and toluene (BXT) selectively.

1.2. PROBLEM STATEMENT AND NOVELTY

Industrialization in an economy not only improves the lives of citizens by providing new products and new employment opportunities, but also has its own challenges. One of the challenges is the production of products that may be harmful to people and also to the environment. Some of these are gasses, some of which are harmful to humans, animals and plants. Some of the gasses may also be highly explosive and or toxic. In some cases, these gasses are harmful even in small quantities (a few parts per million (ppm)).

It is therefore important to look for new materials and sensors with better sensing capability. The most promising materials that may be used as gas sensors are semiconducting metal oxides. It has been proven that miniaturization of devices leads to better performance. It is therefore important, not only that suitable materials are found, but also that their suitable nanostructures are found. In finding suitable nanostructures, the most economical routes must be found and also the safest in terms a number of desirable characteristics such as lower levels of toxicity and also compatibility with other materials that make up the device.

1.3. AIM OF THE STUDY

This work aims to synthesize the doped and undoped Cupric oxide (CuO) using hydrothermal methods and study the effect of doping in order to modulate the intrinsic

or extrinsic defect type and defect concentration that are beneficial to gas sensing properties, with main focus on the volatile organic compound of benzene derivatives i.e. ethylbenzene, p-xylene, toluene (BTX).

1.4. OBJECTIVES OF THE STUDY

The main objective of the study is to synthesize undoped and Zinc (Zn) and tin (Sn) doped CuO using hydrothermal technique and analyse the as synthesized samples using various analytical techniques such as Scanning Electron Microscopy (SEM), Photoluminescence Spectroscopy, X-Ray Diffraction (XRD), Ultra Violet Visible Spectroscopy (UV Vis), Vibrating Sample Magnetometer (VSM) and X-ray Photoelectron Spectroscopy (XPS). Gas sensing applications of the as-synthesized doped and undoped CuO is then performed using a Kenosistec Gas Testing Station at the University of Zululand Physics and Engineering Department.

1.5. DISSERTATION OUTLINE

Chapter I focuses on the background of gas sensing properties of metal oxide based sensors. It also deals with global demands and as well as the structural, optical and electrical properties of CuO nanostructures. The problem statement, aims and objectives form part of this chapter.

Chapter II deals with the literature review on CuO based sensors. This includes the synthesis method employed to prepare the CuO nanostructures and the incorporation of transitional and noble metals in CuO matrix.

Chapter III is focusing on the characterization techniques employed to analyze the CuO metal oxide based sensors.

Chapter IV is devoted on the results and discussions.

Chapter V is a summary and conclusion of the dissertation.

References

[1] B. Kim, J.-H. Ahn, J. Y., C.-S. Lee, Y. C. Kang, F. Abdel-Hady, A. A. Wazzan, and J.-H. Lee. *Highly Selective Xylene Sensor Based on NiO/$NiMoO_4$ Nanocomposite Hierarchical Spheres for Indoor Air Monitoring*. ACS Applied Materials. Interfaces 50, 34603-34611, (2016).

[2] C. H. Feng, C. Wang, H. Zhang, X. Li, C. Wang, P. Cheng, J. Ma, P. Sun, Y. Gao, H. Zhang, Y. Sun, J. Zheng, G. Lu. *Enhanced sensitive and selective xylene sensors using W-doped NiO nanotubes.* Sensors and Actuators B 221, 1475–1482, (2015).

[3] F. Li, S. Ruan, N. Zhang, Y. Yin, S. Guo, Y. Chen, H. Zhang, C. Li. *Synthesis and characterization of Cr-doped WO_3 nanofibers for conductometric sensors with high xylene sensitivity.* Sensors and Actuators B 265, 355–364, (2018).

[4] F. Qu, C. Feng, C. Li, W. Li, and S. Ruan, S. Wen, H. Zhang. *Preparation and Xylene-Sensing Properties of Co_3O_4 Nanofibers.* International Journal of Applied Ceramic Technology (11)4, 619–625, (2014) DOI:10.1111/ijac.12160.

[5] F. Li, S. Guo, J. Shen, L. Shen, D. Sun, B. Wang, Y. Chen, S. Ruan. *Xylene gas sensor based on Au-loaded $WO_3{\cdot}H_2O$ nanocubes with enhanced sensing performance.* Sensors and Actuators B 238, 364–373, (2017).

[6] H. Gao, D. Wei, P. Lin, C. Liu, P. Sun, K. Shimanoe, N. Yamazoe, G. Lu. *The design of excellent xylene gas sensor using Sn-doped NiO hierarchical nanostructure.* Sensors and Actuators B 253, 1152–1162, (2017).

[7] H. Gao, Q. Yu, S. Zhang, T. Wang, P. Sun, H. Lu, F. Liu, X. Yan, F. Liu, X. Liang, Y. Gao, G. Lu. *Nanosheet-assembled NiO microspheres modified by Sn^{2+} ions isovalent interstitial doping for xylene gas sensors.* Sensors and Actuators B 269, 210–222, (2018).

[8] H.-J. Kim, J.-H. Lee. *Highly sensitive and selective gas sensors using p-type oxide semiconductors: Overview*. Sensors and Actuators B 192, 607– 627, (2014).

[9] H.-J. Kim, J.-W. Yoon, K.-Il Choi, H. W. Jang, A. Umar, J.-H. Lee. *Ultra-selective and sensitive detection of xylene and toluene for monitoring indoor air pollution using Cr-doped NiO hierarchical nanostructures.* Nanoscale, 5, 7066, (2013).

[10] H.-S. Woo, C.-H. Kwak, J.-H. Chung, J.-H. Lee. *Co-Doped Branched ZnO Nanowires for Ultra-selective and Sensitive Detection of Xylene*. ACS Applied Materials. Interfaces (2014) dx.doi.org/10.1021/am506674

[11] H.-S. Woo, C.-H. Kwak, J.-H. Chung, J.-H. Lee. Highly selective and sensitive xylene sensors using Ni-doped branched ZnO nanowire networks. Sensors and Actuators B 216, 358–366, (2015).

[12] K. Xu, Y. Yang, T. Yu, C. Yuan. *WO_3 nanofibers anchored by porous $NiCo_2O_4$ nano-sheets for xylene detection*. Ceramics International 44, 21717–21724, (2018).

[13] Y. Cao, P. Hub, W. Pan, Y. Huang, D. Ji. *Methanal and xylene sensors based on ZnO nanoparticles and nano-rods prepared by room-temperature solid-state chemical reaction.* Sensors and Actuators B 134, 462–466, (2008).

[14] Y. Li, Y. Cao, D. Jia, Y. Wang, J. Xie. *Solid-state chemical synthesis of mesoporous Fe_2O_3 nanostructures with enhanced xylene-sensing properties.* Sensors and Actuators B 198, 360–365, (2014).

[15] C. Yang, F. Xiao, J. Wang, X. Su. *3D flower- and 2D sheet-like CuO nanostructures: Microwave-assisted synthesis and application in gas sensors.* Sensors and Actuators B 207 177–185, (2015).

[16] N. Chen, D. Deng, Y. Li, X. Xing, X. Liu, X. Xiao, Y.de Wang. *Xylene sensing performance of WO_3 decorated anatase TiO_2 nanoparticles as a sensing material for gas sensor at low operating temperature.* RSC Advertisement (6), 49692-49701, (2016).

[17] R. O. Yathisha and Y. Arthoba Nayaka. *Structural, optical and electrical properties of zinc incorporated copper oxide nanoparticles: doping effect of Zn*. J Material Sciences 53, 678–691, (2018).

[18] D. N. Oosthuizen, D. E. Motaung, H.C. Swart. *In depth study on the notable room-temperature NO_2 gas sensor based on CuO nanoplatelets prepared by sonochemical method: Comparison of various bases*. Sensors and Actuators B: Chemical 266, 761-772, (2018).

[19] A. Sharma, M Varshney, HT Kyun, KH Chae, HJ Shin. *X-ray absorption spectroscopy study and photocatalyst application of CuO and $Cu_{0.9}Ti_{0.1}O$ nanoparticles*. Currant Applied Physics. 15, 1148, (2015).

[20] X. Li, W Guo, Y Liu, W He, Z Xiao. *Spinel $LiNi_{0.5}$- $Mn_{1.5}O_4$ as superior electrode materials for lithium-ion batteries: Ionic liquid assisted synthesis and the effect of CuO coating*. Electrochimica Acta 116, 278, (2014).

[21] H Siddiqui, MS Qureshi, FZ Haque. *Valuation of copper oxide (CuO) nanoflakes for its suitability as an absorbing material in solar cells fabrication*. Optik 127, 3713, (2016).

[22] R Etefagh, E Azhir, N Shahtahmasebi. *Synthesis of CuO nanoparticles and fabrication of nanostructural layer biosensors for detecting Aspergillus niger fungi*. Sci Iran F 20, (3), 1055, (2013).

[23] M.A Kumar, S.M Kumaran. *Effect of Ni doping on electrical, photoluminescence and magnetic behaviour of Cu doped ZnO nanoparticles*. J. Lumin. 162, 97, (2015)

[24] G.K. Williamson, W.H. Hall. *X-ray line broadening from filed aluminium and wolfram*. Acta Metall, 1, 22-31, (1953).

[25] N. Zhang, S. Ruan, J. Han, Y. Yin, X. Li, C. Liu, S. Adimi, S. Wen, Y. Xu, *Oxygen vacancies dominated CuO@$ZnFe_2O_4$ yolk-shell microspheres for robust and selective detection of xylene*, Sensors and Actuators: B 295, 117-126, (2019).

[26] H. Gao, J. GuO, Y. Li, C. Xie, X. Li, L. Liu, Y. Chen, P. Sun, F. Liu, X. Yan, F. Liu, G. Lu. *Highly selective and sensitive xylene gas sensor fabricated from NiO/$NiCr_2O_4$ p-p nanoparticles*. Sensors & Actuators: B. Chemical 284, 305-315, (2019).

CHAPTER II

2.Applications of CuO Nanostructures

Cupric oxide (CuO) has been considered as the most interesting transition metal oxides because of its properties as a p-type semiconductor with a narrow band gap (1.2 eV in bulk) and as the foundation of several high-temperature superconductors and giant magneto resistance materials **[32, 33–38]**. CuO nanostructures have a superior physical and chemical properties that extraordinarily different from those of their micro or bulk structures. CuO nanostructures is considered as electrode materials for the next-generation rechargeable lithium-ion batteries (LIBs) due to their high theoretical capacity, safety, and environmental friendliness **[39]**.

They are considered promising candidate for solar cells due to their high solar absorbance, low thermal emittance, good electrical properties, and high carrier concentration **[40]**. CuO nanostructures have been used in numerous applications, such as gas sensors **[41]**, bio-sensors **[42]**, nanofluid **[43]**, photodetectors **[44]**, energetic materials (EMs) **[45]**, field emissions **[46]**, supercapacitors **[47]**, removal of inorganic pollutants **[48, 49]**, photocatalysis **[50]**, and magnetic storage media **[51]** and have been demonstrated to be used to synthesize organic–inorganic nanocomposites with high thermal conductivity, high electrical conductivity, high mechanical strength, high-temperature durability **[32, 33, 52, 53]**. In this work, we investigate CuO as gas sensor

2.1. Brief History on Gas Sensing

The first development of a gas sensor based on SnO_2 and ZnO in 1962 by T. Seiyama et al. **[1, 2]** and N. Taguchi **[3]**, attracted interest toward the development of these small dimensional devices materials for gas sensing practical applications.Later, effort to introduce small additives such as nobel metals i.e. Pt, Ru, and Pd has been made to improve the sensitivity and selectivity of the sensor **[4-7]**. These semiconducting metal oxides should be able to continuously monitor these toxic gases, vapours and odours in different environments such as work places, homes and offices.Even though great efforts to improve on the gas sensing properties of these sensor materials has been made, there are many challenges associated with these sensing properties and technologies in real practical situations that are still in existance. Some of these challenges are inaccuracies, response time, reliable, low-maintenance and selectivity. Due to huge commercial demands to find excellent sensors ,there are several attempts to find new less complex materials with excellent sensing properties.

2.2. Global Demand for Gas sensors

The world has become more sophisticated and complex. Therefore, stringent environmental compliance and regulation enforced in different regions along with growing awareness about environmental degradation and pollution has led to strong growth of the global emission monitoring systems market. Sensors in many of its forms have become part of our daily lives. Gas sensors, too, have received demands to the industrial processes causing huge damage in pollutions resulting in global climate change due to various gas species released to the atmosphere. So, market assessment

involves the identification of these good potential sensors for a target gas or gases and validate the technical readiness level of the sensor technology. According to a report, “Gas Sensors Market – Global Industry Size, Share, Trends, Analysis and Forecast, 2017-2025,” an estimated value of US$2.32 billion by 2018 is expected for the global sensors market, at a compound annual growth rate of 7.5% between these year range, 2017-2025 **[8]**.

Metal oxide semiconductors for gas sensor rely on the chemical sensitivity of their surfaces during the interaction with an analyte for gas-sensing applications.These metal oxides are either n-type or p-type semiconductors. This means that the majority charge carriers in the surface are either electrons or holes. A sensor detects a change in its electrical resistance or current due to the presence of a particular gas in the atmosphere. One important aspect in the chemiresistor gas sensor is the potential energy barriers between grains contacts. In order for a gas sensor to perform its function, there is a receptor and transducer functions. The receptor function acknowledges the presence of a chemical substance in the surface of the semiconductor and the transducer function transduces the chemical reaction signal between the semiconductor’s surface and the chemical substance into an electric output signal.

2.3. Bulk Properties of CuO

In the variety of copper oxides, the cupric oxide (CuO) phase is well known as a gas-sensitive material. The CuO is a p-type semiconductor with low electrical resistance

values in air however high electrical resistance in vacuum. It belongs to the d-block with $3d^9$ electronic configuration and assumes an anti-ferromagnetic ordering in the ground state with a bandgap of about 1.2 eV **[9]**. It is noteworthy to mention that this optical bandgap is identified as originating from charge-transfer as oppose to being d→d transitions, its electrical conductivity decreases when exposed to the reducing environment or gaseous containing environment.

As a sensing element, the material sensitivity changes drastically depending on temperature and dopants. In its pure form It is highly sensitive to VOCs and BTEX gases at elevated temperatures but becomes less sensitive upon the incorporation small dopant of Zn at atomic level percentages. However, at higher atomic percentages its sensitivity is so insignificant. The Sn-doping completely diminishes the sensitivity and become insensitive to these gases. The situation is different for conventional gases like NO_2, NO, CO_2, CO, even at room temperatures.

2.4. Physical and Chemical properties of Copper Oxide (CuO)

Cupric oxide (CuO) is a brownish-black powder which is chemically and thermodynamic compound with band gap of 1.2 eV in its bulk form. CuO is antiferromagnetic material at 213 K and paramagnetic at 230 K. Cupric oxide (CuO) crystal has monoclinic structure as shown in **Figure 2.1** which belong to C_{2h}^6symmetry group with four formula units per unit cell. It has 4 coordination number of copper atom, which is linked to four oxygen neighbour atoms in a square planar configuration along (110) plane. Crystallized divalent copper surroundings are very distorted by a strong Jahn-Teller effect which leads to a more stable square planar groups. The Cu-O bond lengths in this plane are 1.88 and 1.96 Å, respectively, which are larger than those in the cuprous oxide **[10]**.

The contributors to the formation of CuO crystal structure are Cu^{2+} and O^{2-} and the unit cell lattice parameters of cupric oxide **[11]** are presented in **Table 1** below.

Table 2.1.*Crystallographic properties of CuO and some physics constants of CuO* ***[10-12]***

SPACE GROUP	**C2/c (No. 15)**
Unit cell	a = 4.68.37 A b = 3.4226 A c = 5.1288 A β = 99.54^{0} a = y = 90^{0}
Cell volume	81.08 A^3
Cell content	4CuO
Formula weight	79.57
Density	6.515 g cm^{-3}
Distances Cu-O O-O Cu-Cu	 1.96 A 2.62 A 2.90 A

Melting point	1201^0C

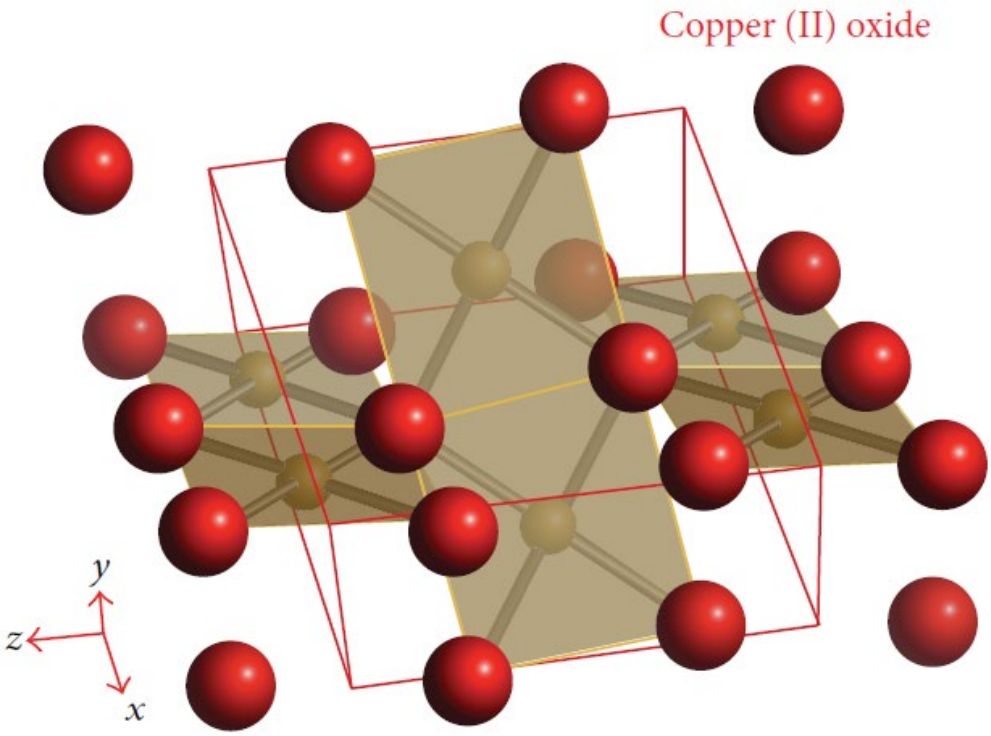

Figure 2.1. *Crystal structure of CuO* ***[12]***

CuO is also being considered as a good candidate material to be used in nanofluid which are introduced being used in many applications these days such as electronic, nuclear reactor, biomedical, automotive, and industrial cooling due to its thermal conductivity properties **[13]**.

References

[1]. T. Seiyama, A. Kato, K. Fujiishi, M. Nagatani, *A New Detector for Gaseous Components Using Semiconductive Thin Films*. Analytical Chemistry, 34, 1502-1503 (1962).

[2]. T. Seiyama, S. Kagawa, *Study on a detector for gaseous components using semiconductive thin films*, Anal. Chem. 38 (8) 1069–1073 (1966).

[3]. N. Taguchi, Gas Detecting Device, US Patent 3, 695, 848 (1972).

[4]. N. Yamazoe, G. Sakai, K. Shimanoe, *Oxide semiconductor gas sensors*, Catal. Surv. Asia 7 63-75 (2003).

[5]. N. Yamazoe, Y. Kurokawa, T. Seiyama, *Effects of additives on semiconductor gas sensors*, Sensor. Actuator. 4 283-289 (1983).

[6]. P. Tyagi, A. Sharma, M. Tomar, V. Gupta, Metal oxide catalyst assisted SnO_2 thin film based SO_2 gas sensor, Chem. Sensors, 4, 18, 1-7 (2014).

[7]. A. Sharma, M. Tomar, V. Gupta, *Effect of WO_3 catalyst nanoclusters towards NO_2 sensing characteristics of SnO_2 films*, J. Nanosci. Lett. 2 27 (2014).

[8]. *Report. Level Sensor Market Size, Share & Trends Analysis Report by Technology (Contact Type/Point Level, Non-Contact Type/Continuous Level), By Application* (Automotive, Consumer Electronics, Healthcare), And Segment Forecasts, 2018-2025 ID: 978-1-68038-230-3

[9]. P. Raksa, A.Gardchareon, T. Chairuangsri, P.Mangkorntong, N. Mangkorntong, and S. Choopun, *Ethanol sensing properties of CuO nanowires prepared by an oxidation reaction*, Ceramics International, vol. 35, no. 2, pp. 649–652, (2009).

[10]. W. Y. Ching, Y.-N. Xu, and K. W. Wong, *Ground-state and optical properties of Cu_2O and CuO crystals*, Physical Review B, vol. 40, no. 11, pp. 7684–7695, (1989).

[11]. Y. Cudennec and A. Lecerf, *The transformation of $Cu(OH)_2$ into CuO, revisited*, Solid State Sciences, vol. 5, no. 11-12, pp. 1471–1474, (2003).

[12]. T. H Tran and V. T Nguyen, *Copper Oxide Nanomaterials Prepared by Solution Methods, Some Properties, and Potential Applications:* A Brief Review, Hindawi Publishing Corporation International Scholarly Research Notices Volume 2014, Article ID 856592, 14 pages http://dx.doi.org/10.1155/2014/856592

[13]. Rahman MM, Saleh Ahammad aJ, Jin J-H, Ahn SJ, Lee J-J. *A comprehensive review of glucose biosensors based on nanostructured metal-oxides.* Sensors (Basel, Switzerland); 10: 4855–86 (2010).

CHAPTER III

3.1. Synthesis of CuO Nanostructures

A brief overview of several synthetic methods for the engineering manufacturing of the nanostructured cuprous oxide materials is discussed. This section is meant to provide a good reason for the selection of our synthetic methodology for our copper oxide nanostructures. In nanotechnology, large scale manufacturing of nanostructures still remains a challenge. The synthesis methods differ in the degree of complexity, cost, manufacturability, and environmental hazard **[54]**.

The manipulation of well-controlled synthesis and engineering of nanostructured transition metal oxides with different sizes, shapes, chemical compositions, and structures is very crucial in the advancement of nanoscience and nanotechnology field. There are enormous physical and chemical synthetic methods or techniques that are widely accepted by material researchers for the fundamental investigation for realizing possible applications of nanoscale materials. Wet chemistry or solution-based method is a scalable method that is used to synthesize nanostructures of CuO with different morphologies, sizes and shapes.

The synthesis methods used to synthesize undoped and doped CuO nanoparticles and nanostructures are sol-gel, spray pyrolysis, precipitation, solvothermal, aqueous chemical growth, hydrothermal, and electrochemical methods **[55–60]** and microwave

irradiation approach [61–63] with diverse morphologies, sizes, and dimensions using various chemical, physical, or chemistry physics combined strategies. These synthesis methods allow for the control of different parameters such as shape, particle size, size distribution, and composition. In this work we focus only on the solution based method (hydrothermal synthesis method) to synthesis copper (II)-oxide (Cu=O) nanostructures with different morphologies, sizes, shapes.

The possibility to use low cost and high-throughput equipment, low wastage of raw materials, high uniformity of size and shape of the nanoproduct and can easily be tailored. Doping can also be easily achieved with this synthesis method.

3.2 Characterization Techniques

After the target material has been deposited onto the substrate where the thin film is formed, the properties of the thin film (crystallinity, morphology, composition, surface roughness and thickness) are investigated. In this study the characterization techniques like X-ray diffraction, scanning electron microscopy, energy dispersive spectroscopy, atomic force microscopy and Rutherford backscattering spectroscopy were utilized to investigate the properties of the deposited thin films.

3.3X-Ray Diffraction (XRD)

The photograph of the X-Ray Diffraction (XRD) unit presented in **Figure 3.1** is a non-destructive analytical technique which can give the information about the crystallographic structure and chemical composition of materials and thin films. This

technique is based on monitoring the scattered intensity of an x-ray beam hitting a sample as a function of incident and scattered angle, polarization, and wavelength or energy **[1-3]**. In crystalline structures the atoms are arranged in a periodic lattice with planar (d-spacing). Constructive interference of x-rays occurs when the Bragg **[4]** condition is satisfied following eqn (3.1);

$$n\lambda = 2d_{(hkl)} \sin\theta_B \tag{3.1}$$

where *n* is an integer (normally set as *n* = 1), *θ* is the angle of incidence and d is the spacing between the diffracted planes. Therefore, by scanning a range of angle of incidence, the characteristic *d*-spacing of the crystal can be identified **[5]**. The x-ray diffraction pattern of the synthesized material is qualitatively compared with a reference database to identify the crystallographic phase. Reference patterns are generated from powder samples, where all possible crystallographic orientations are present. Further analysis of XRD patterns gives much information about the structure of the sample, including the crystal size, amorphous component and degree of stress in the lattice.

X-Ray Diffraction was carried out using a Bruker AXS D8 Advance X-ray diffractometer with primary monochromatic high intensity Cu Kα (λ=1.541 Å) radiation with a PSD (position sensitive detector) detector at the scan step of 0.0070 and scan speed of 1 step/s. The Scherer equation shown below can be used to calculate the crystallite size, *D*, along a given plane as demonstrated by eqn (3.2);

$$D = \frac{K\lambda}{B\cos\theta_B}$$

(3.2)

where λ is the x-ray wavelength (in nm), K is a constant (usually assumed to be close to 1 or 0.89), B is the full-width-half-maximum (FWHM) value of the diffraction signal (in radians), and θ_B the angle at which the peak of the signal occurs.

(a)

(b)

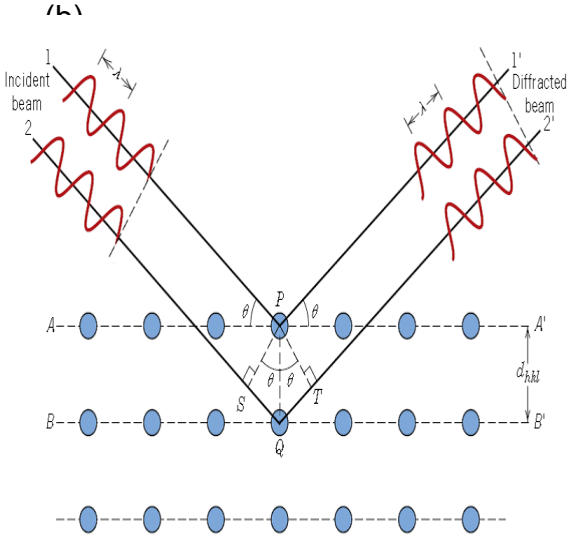

Figure 3. 1. *Bruker's X-ray diffraction D8-Discover instrument and (b) Interaction of incident X-ray beam with the crystalline sample* ***[6]****.*

3.4 Scanning Electron Microscope (SEM)

The scanning electron microscope reveals information about the morphology, chemical composition, of the samples by scanning the surface with energetic beam of electrons. SEM is equipped, with Energy Dispersive Spectroscopy (EDS) **[7]** is used to identify and quantify elements present on a sample. It can also give the information about the

thickness of the sample. **Figure 3.2a** shows the SEM of the University of Zululand in the Physics and Engineering Department that was used in this investigation. The main components of SEM, as shown in **Figure 3.2b)** are the electron source (electron gun), microscope column, magnetic lenses, scanning coils, electron detectors, sample chamber, computer and display screen to view the images **[8]**. The transmission electron microscope (TEM), in Figure 3.3, provides the information about the structure shape and size of the samples.

(a) (b)

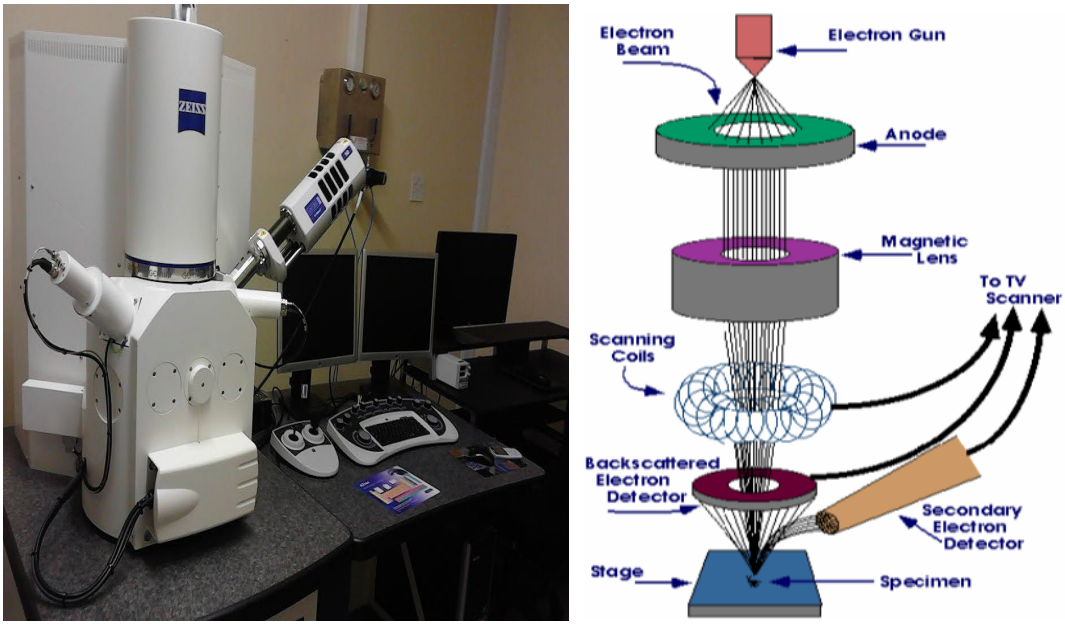

Figure 3. 2. *(a) SEM of the University of Zululand in the Physics and Engineering Department. (b) Schematic illustration of the basic components of the SEM* ***[9]****.*

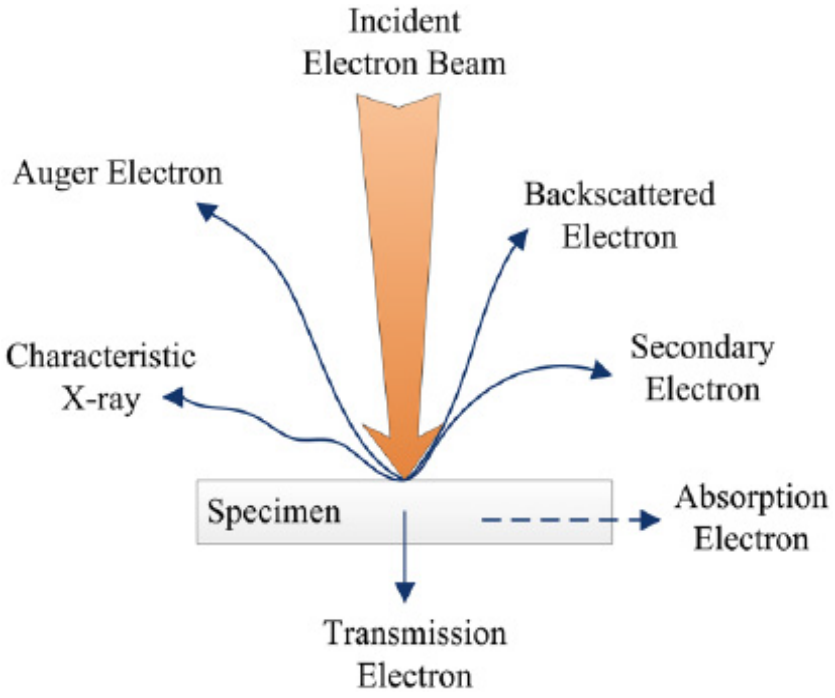

Figure 3. 3. *The Schematic representation of the interaction of the incident beam and radiation signals generated during interaction* ***[10]****.*

In addition to SEM equipped with EDS and XRD analysis techniques, X-ray photoelectron spectroscopy (XPS) which is a nondestructive quantitative technique is used to measure the elemental composition and to determine the binding states of the elements in the compound found in the sample.

3.5 Ultraviolet Visible Spectroscopy (UV VIS) on CuO

In nanomaterials, there are several methods to be used to characterize the optical properties and to estimate the bandgap of a synthesized material. The quick and most convenient techniques which is non-destructive to investigate the energy structure and the optical properties of a semiconducting materials is UV-vis absorption spectroscopy. In this optical characterization technique the photons with energies equal or greater

than the band gap of the material get absorbed and excite electrons from the high occupied molecular orbital (HOMO) to the low unoccupied molecular orbital (LUMO). Photons with lower energies get transmitted therefore they do not excite electrons in the material. The optical bandgap of semiconductor material is estimated and calculated from the absorption spectra by using Tauc's relation **[16]**

$$\alpha h\upsilon = (h\upsilon - Eg)^n \quad (3.3)$$

$$\alpha = -\frac{\ln(x)}{d} \quad (3.4)$$

$$h\upsilon = E = h\frac{c}{\lambda} \quad (3.5)$$

Where x, λ, and c are the absobance values, wavelength and the speed of light in vacuum, respectively. E or $h\upsilon$ is the energy of incident photon and *n* is the exponent factor that determines the type of electronic transition causing the absorption and can take the values ½ and 2 ; depending whether transition is direct or indirect, respectively. Bandgap is determined from the intercept of the tangent straight line with the horizontal axis.Some groups have reported significant blue shift values of the band gap (up to 1.7 eV) **[17]** in the absorption edge compared with the bandgap of bulk CuO material, which was explained by the quantum confinement effect in these nanostructures. **Figure 3.4** is the schematic diagram of the UV Vis spectroscopy.

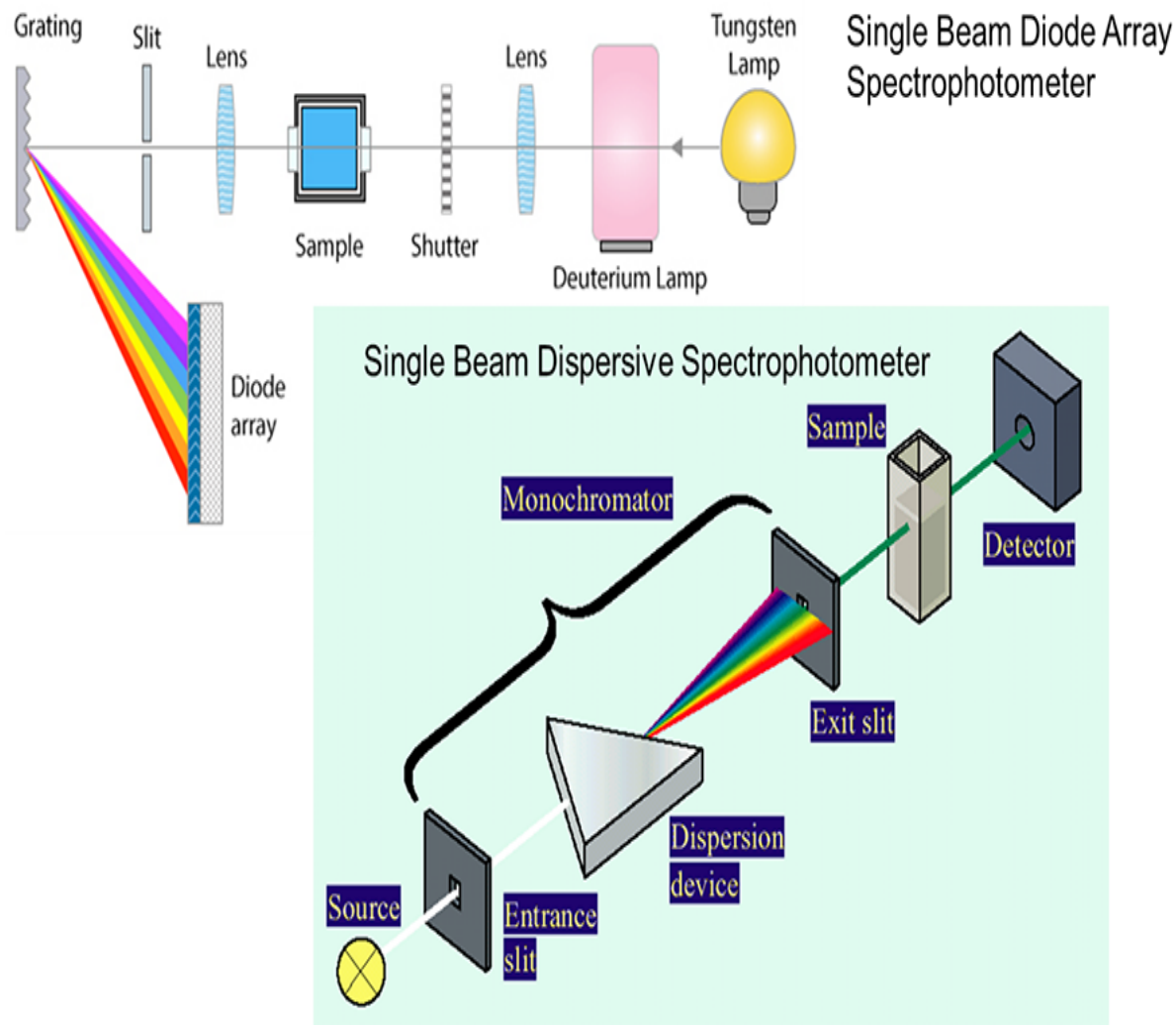

Figure 3. 4. *The Schematic diagram of UV VIS spectroscopy* ***[ref]***

3.6Photoluminescence Spectroscopy (PL)

Photoluminescence spectroscopy (shown in **Figure 3.5**) is a nondestructive technique that is used to investigate optical properties of semiconductor materials. It uses a photo-excitation process whereby photons, stimulate the emission of a photon from any matter. Basically, light is directed onto a sample, where it is absorbed resulting in photo-excitation process. This process stimulates the atoms of the material to be excited, and will then release , (photons) as it relaxes and returns to back to a de-

excited state. It reveals information about the bandgap of the material, impurity level and defect on the material, electronenergy- hole recombination and also molecular structure and crystallinity of the material being investigated.

There are several photoluminescence bands generally reported for CuO nanostructures which expand from UV to near IR region; however, the most frequent peaks fall in the region from 400 to 600 nm. Generally, the deep level emission in CuO consists of a green emission at around 605 nm and a near-yellow emission at around 680 nm. CuO is intrinsically a p type semiconductor due to the existence of Cu vacancies. Theoretical calculations have proven that although Cu vacancies are the most stable defects in CuO, they do not make any changes in the electronic structures of CuO. O_{Cu} antisite defects were reported to be responsible for these emissions and the formation energy was reported to be almost similar to the formation energy of Cu vacancies [18]. The green emission is assigned to the singly ionized oxygen vacancies while the yellow or red emission has been related to the interstitial metal ion in the oxide. The evolution of green and yellow bands in CuO was competitive with each other. The blue shift of the near band edge transition was attributed to the enhancement of the quantum confinement effect resulting from the decrease in the dimensional structure and the size of the nanoparticles.

Vila et al. **[19]** reported the luminescence bands cantered around 1.33, 1.23, and 1.11 eV in CuO nanomaterial and suggested that the emission with highest energy corresponds to near band edge transition in CuO while the two emissions were most probably introduced by oxygen vacancies and oxygen on copper antisite defects **[18-21]**. Santra et al. **[12]** reported the near band edge emission at 395nm in the violet

region while Aslani et al. **[22]** reported near band edge emission at 300 nm. Mageshwari and Sathvamoorthy **[23]** reported several photoluminescence peaks at 325, 339, and 356 nm and explained the difference photoluminescence emission peaks of CuO as agreed with earlier reports by various sizes and shapes of CuO nanostructures. These studies indicated that the luminescence properties of CuO were strongly dependent on the morphology of the nanocrystals. Gizhevsk et al. **[24]** reported the photoluminescence board emission bands centred around 305 nm (4.07 eV), 505nm (2.46 eV), and 606 nm (2.05 eV) **[22, 25-28]** and indicated that these bands were due to the temperatures and annealing time during sample of CuO nanocrystals.

PL intensities of the 305 nm (4.07 eV) band were seen to increase with the increasing temperature treatment and were explained by the enhancement of the crystallinity of the sample.

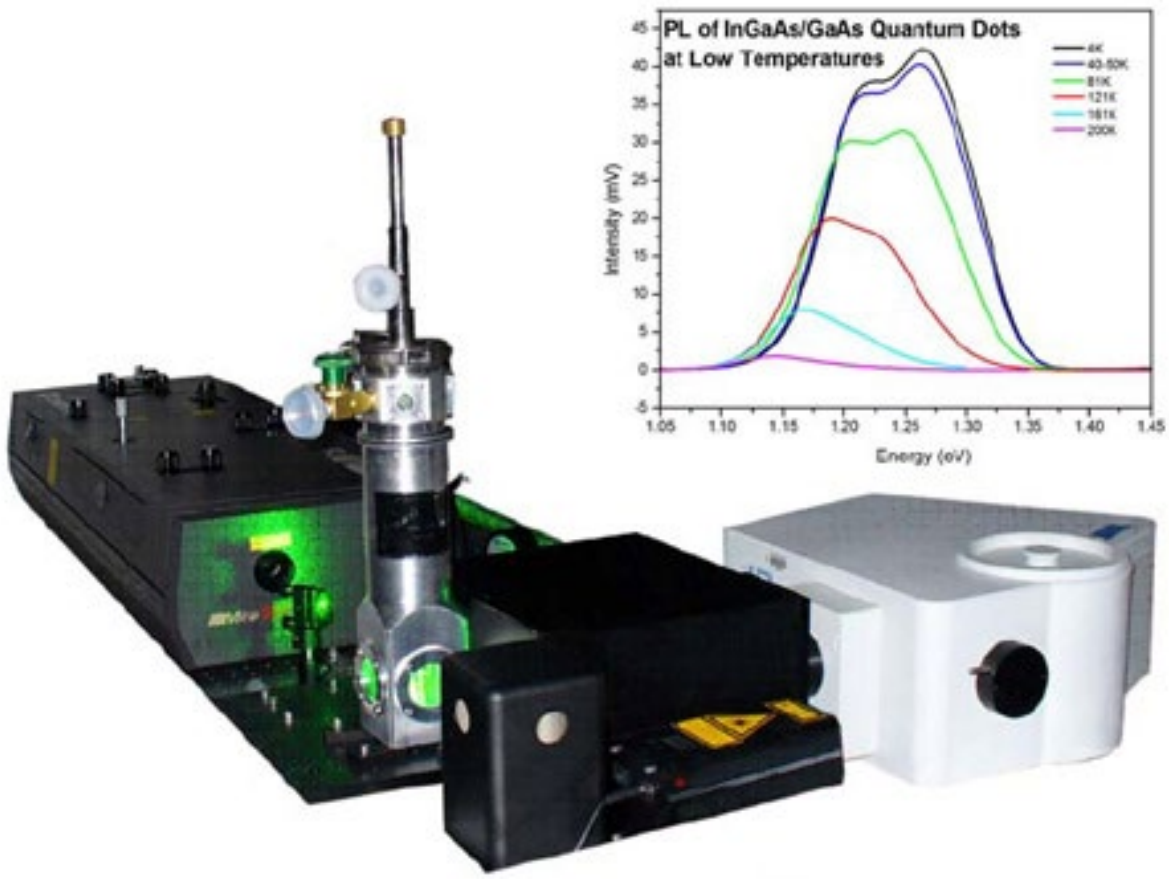

Figure 3. 5. *The Diagram of a Photoluminescence spectroscopy and the example of the signal obtained from it on the sample.*

3.7Vibrating Sample Magnetometer (VSM) Spectroscopy

The Magnetic Properties aspects of CuO nanomaterials have been investigated over the years and showed interesting and unique magnetic properties. Kimura et al. **[29]** reported that CuO, which is different from other antiferromagnetic transition metal monoxides such as NiO, MnO, and CoO, shows magnetic order above Neel temperature. V. Bisht et al **[30]** reported that the magnetic properties of CuO is temperature dependant and have shown two Neel temperature with two antiferromagnetic transition at 213 K and 230 K, where the 213 K transition was related

to commensurate to incommensurate transition, while the one at 230K was attributed to incommensurate to paramagnetic transition.

In this work we employ VSM (shown in **Figure 3.6** below) which is a very sensitive technique used to measure the magnetic moment of a sample when it is vibrating *perpendicularly* to a uniform magnetizing field. It uses the principle of Faraday's law of magnetic induction. In this technique the sample is placed under a uniform magnetic field H, which induces a magnetization M in the sample. The hysteresis loop shows the “history dependent” nature of magnetization of a ferromagnetic material. Once the material has been driven to saturation, the magnetizing field can then be dropped to zero and the material will retain most of its magnetization as can be seen on the **Figure 3.6c)** below.

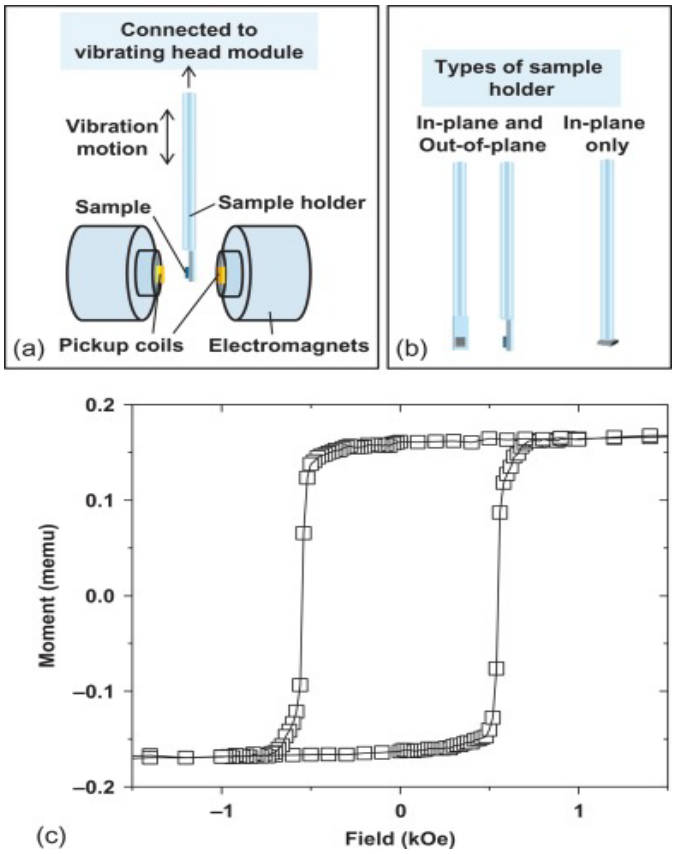

Figure 3. 6. *The Schematic diagram of: (a) part of the VSM setup and (b) types of sample holder used in VSM. (c) Typical magnetization curve which can be obtained using VSM showing the out-of-plane magnetic moment versus applied magnetic field for* $[Co(0.5\ nm)/Pd(3\ nm)]_{10}$ *film deposited using sputter deposition* ***[31]****.*

3.8Sample preparation Synthesis procedure

The chemicals were purchased from Sigma-Aldrich and used as received with a high purity, >98%. Pure ZnO and CuO and as well as Zn doped CuO nanoplatelets were synthesized using the hydrothermal method. About 0.2 M of $Cu(NO_3)_2{\cdot}xH_2O$ [Copper(II) Nitrate Hydrate from Sigma-Aldrich, reagent grade >98% purity] was used to synthesize pure CuO samples while the cupric oxide decorated with Zn samples (0.1, 0.25, 0.5, 1.0, and 2.0 at. %) were synthesized using appropriate quantities of both $Cu(NO_3)_2{\cdot}xH_2O$ and $Zn(NO_2)_3{\cdot}6H_2O$ (Zinc nitrate hexahydrate) precursors in a volume

of 125 mL. During the sample preparation, the pH was adjusted to 10.5 to initiate and allow CuO metal oxide nucleation by adding 1.0 M sodium hydroxide (NaOH) drop wise under vigorous stirring at room temperature. The literature suggests that the pH adjustment creates different size, shape and morphology. Therefore, the pH 10.5 was reported to be the favorable one for the nucleation of ZnO nanoplatelets **[1]**. After controlling pH, the solution was then kept under vigorous stirring for aging of 2 h. Subsequently, the volume of 125 mL was transferred to a 200 mL stainless steel autoclave reactor vessel (Anton Parr) and placed in a laboratory oven at 150 °C for 12 h. The black solid precipitates at the bottom of the container were collected. The removal of the residual salts was done by several rinse-centrifugation cycles using distilled water and ethanol. The products were dried overnight at 90 °C. To ensure that we achieve the correct phase, the samples were annealed in air at 200 °C for 2 h.

3.9.1Hydrothermal Synthesis Method

Hydrothermal synthesis is a solution reaction-based method which is commonly used for synthesis of nanomaterials. This synthesis approach allows the formation of well controlled morphology, size and shapes of nanomaterials from room temperature to very high temperatures. The literature suggests that many types of nanomaterials with different shapes and sizes have been successfully synthesized using this synthesis approach. There are significant advantages of hydrothermal synthesis method over others such as the generation of unstable nanomaterial at elevated temperatures and can enable the production of nanomaterials at high vapor pressures with minimum loss of materials. The compositions of nanomaterials to be synthesized can be well controlled in hydrothermal synthesis through liquid phase or multiphase chemical

reactions. Hydrothermal synthesis of nanoparticles allows the production of several shapes and sizes of nanoscale particles such as nanorods, nanotubes, hollow nanospheres, and graphene nanosheets.

This research method allowed Cao et al. **[64]** to synthesize Cu, Cu_2O, and CuO nanotubes as well as nanorods. Cheng et al. **[65]** managed to use hydrothermal method to synthesized CuO nanorods in a large scale using the same method and proved that the concentration of surfactant critically influences the morphology of CuO nanorods while Gao et al. **[66]** reported that the crystalline structures and morphology of CuO nanorods depend on the temperature. The same method allowed Dar et al. **[67]** to synthesize CuO nanoneedles. This method have the advantage to tailor the synthesize nanostructures. **Figure 3.7** illustrates the schematic diagram of a typical hydrothermal synthesis for CuO nanostructures.

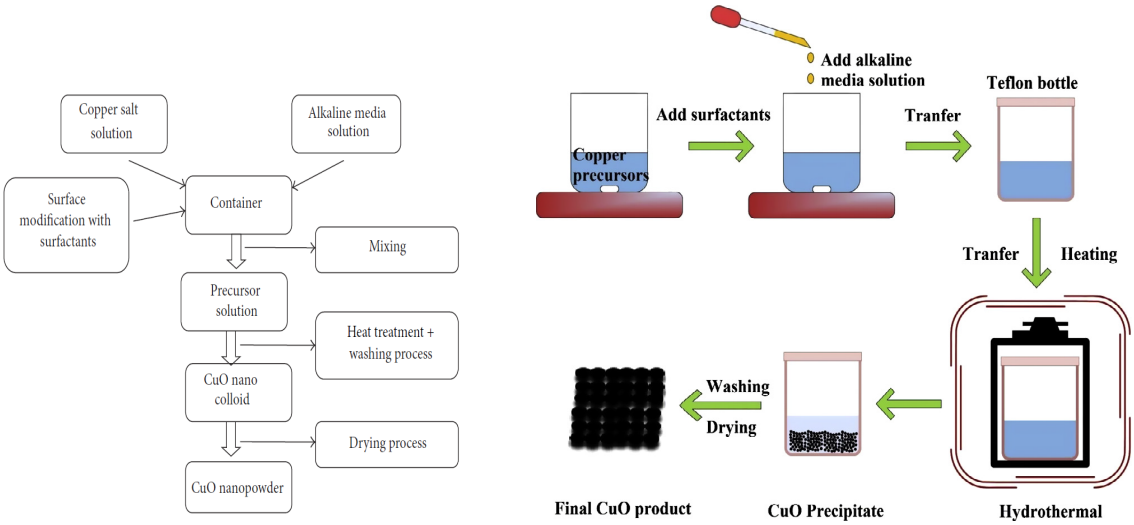

Figure 3. 7. *The Schematic diagram of a typical hydrothermal synthesis for CuO nanostructures* ***[68]****.*

3.11Gas Sensing Mechanism Semiconducting Metal Oxides

The metal oxide gas sensor works on the principle of chemiresistance which is the change in electrical conductivity or resistivity of semiconducting metal oxide on exposure to a target gas. Basically, the gas molecules interact with the metal oxide either act as a donor or acceptor of charge carriers which then changes the resistivity of the metal oxide as shown in **Figure 3.8**. The increase or decrease of resistance of the metal oxide thin film depends on the type of majority carriers in the semiconducting metal oxide and the nature of gas molecules in an ambient atmosphere. The gas either be oxidizing or reducing. In *n*-type materials, oxidizing gases increase the resistance of semiconducting metal oxide while reducing gases decrease and are correspondingly opposite for *p*-type materials **[69]**. This describes the behavior of the metal oxide gas sensor. The metal oxide sensors in nanoscale plays a significant role in the development of gas sensors **[70]**.

The chemiresistance property of the metal oxides can be related to the width of the space charge region formed on the crystallites due to the transfer of electrons during the adsorption and desorption of gas molecules. The width of the space charge region acts as a potential barrier in the conduction process between the grains and encourages changes in the Fermi level positioning. The process of creation and annihilation of electrons form the conduction band results in band bending and Fermi level modulation. The oxidizing gas when interacted with *n*-type material, the band bends upward due to the depletion of electrons. When the reducing gas interact with the

p-type material the band bends downward due to the accumulation of electrons. Therefore, one can conclude by saying the direct relation between space charge region and band bending depends on the carrier concentrations in the grain. Since the gas sensing is based on the change of resistance/current of the metal oxide material upon exposure to a certain gas or gases.

The adsorption, oxidation and desorption process is generally connected to the oxygen species (O^{2-}, O^{-}, and O_2^{-}) that get adsorbed on the surface of a semiconducting metal oxide **[71-77]**. During these reactions, the surface of a p-type semiconducting transition metal oxide such as CuO adsorbs these oxygen molecules that are ionized by conduction band electrons to form a hole carrier species layer. The mobility carriers in CuO-based sensors are mostly holes, which lead to a decrease in the resistance of the sensor. This process is opposite to some n-type semiconductors such as WO_3 for the same reducing gas **[78, 79]**.

The adsorption-oxidation-desorption reactions can be described using the following equations depending on the operating temperature:

$$O_{2(gas)} \leftrightarrow O_{2(ads)} \tag{3.6}$$

$$O_{2(ads)} + e^{-} \rightarrow O^{-}_{2(ads)} \text{ [T < 100°C]} \tag{3.7}$$

$$O^{-}_{2(ads)} + 2e^{-} \rightarrow 2O^{-}_{(ads)} \text{[100°C < T < 300°C]} \tag{3.8}$$

$$O^{-}_{(ads)} + e^{-} \rightarrow O^{2-}_{(ads)} \quad \text{[T > 300°C]} \tag{3.9}$$

The target gas molecules react with the ionic oxygen species chemisorbed on the surface of the p-type such as CuO, leading to narrow channel and high resistance states. Therefore, the sensing function mostly depends on the resistance change due to interactions of these chemisorbed oxygen species with the target gas, resulting in the release of electrons back into the conduction band of the sensor. An enhanced sensing performance is a result of an efficient process to adsorb and ionize these oxygen molecules. Crystallite size and surface area are reported to be responsible for enhanced sensing performance of metal oxide gas sensors **[73, 80]**.

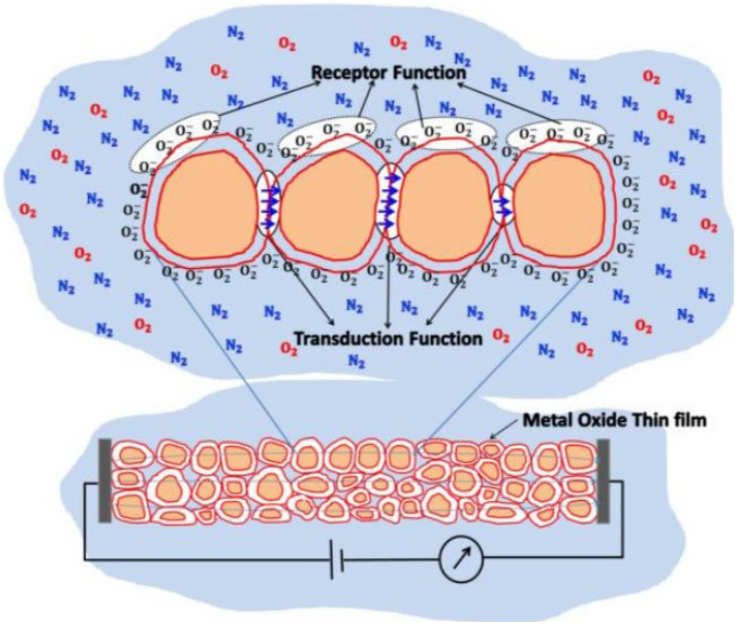

Figure 3. 8. *The Schematic of metal oxide thin film gas sensor* ***[ref]****.*

The sensitivity for the n-type semiconductor is calculated as follows:

$$S = \frac{R_{air}}{R_{gas}} \tag{3.10}$$

This equation is for an n-type semiconductor, while the one for the p-type semiconductor is calculated using the formula:

$$S = \frac{R_{gas}}{R_{air}}$$

The percentage is calculated as;

$S(\%) = \left(\frac{R_{air} - R_{gas}}{R_{air}} \right) \times 100$, for n-type semiconductor

R_{air} is the resistance of the gas sensor before passing the gas and R_{gas} is that after passing the gas and reaching the saturation value [81]. It is well known that the fundamental sensing mechanism of semiconductor based gas sensors relies on a change in electrical conductivity due to the interaction between the surface complexes such as O^-, O_2^-, reactive chemical species (OH^-), and gas molecules to be detected.

References

[1]. Johansson, S. A. E., Campbell, J. L. and K. G. Malmqvist, *Particle Induced X-ray Emission Spectrometry*, Wiley, New York, (1995).

[2]. Callister, W. D. *Materials science and engineering and introduction,* 6th ed., John Wiley & Sons, Inc., Department of Metallurgical engineering, University of Utah, (2003).

[3]. Askeland, D. R. *The science and engineering of materials*, Alternate edition, PWS-KENT publishing company, University of Missouri-Rolla, (1994).

[4]. [www 2] https://www.chem.uci.edu/~lawm/263 4.pdf (20/03/2017).

[5]. Fultz, B. and Howe, J. *Transmission Electron Microscopy and Diffractometry of Materials*, 3rd ed., Springer Berlin Heidelberg (2008).

[6]. B. Cheney. *Introduction to Scanning Electron Microscopy*. Materials Engineering department San Jose State 2-12, (2007).

[7]. Marburger, W. G. and Hoffman, C. W. *Physics for our times,* New York:McGraw-Hill Book company (1958).

[8]. [www 6] http://www.purdue.edu/ehps/rem/rs/sem.htm (03/04/2017).

[9]. [www 6] http://www.purdue.edu/ehps/rem/rs/sem.htm (03/04/2017).

[10].[www7]http://cdn.iopscience.com/images/09574484/25/18/185705/Full/nano490588f2_online.jpg (03/04/2017).

[11]. P. Raksa, A.Gardchareon, T. Chairuangsri, P.Mangkorntong,N. Mangkorntong, and S.Choopun, *Ethanol sensing properties of CuO nanowires prepared by an oxidation reaction*, Ceramics International, vol. 35, no. 2, 649–652, (2009).

[12]. K. Santra, C. K. Sarkar, M. K. Mukherjee, and B. Ghosh, *Copper oxide thin films grown by plasma evaporation method*, Thin Solid Films, vol. 213, no. 2, 226–229, (1992).

[13]. S. Cho, *Optical and electrical properties of CuO thin films deposited at several growth temperatures by reactive RF magnetron sputtering*, Metals and Materials International, vol. 19, no. 6, 1327–1331, (2013).

[14]. H.-H. Lin, C.-Y. Wang, H. C. Shih, J.-M. Chen, and C.-T. Hsieh, *Characterizing well-ordered CuO nanofibrils synthesized through gas-solid reactions*, Journal of Applied Physics, vol. 95, no. 10, 5889–5895, (2004).

[15]. M. Kaur, K. P. Muthe, S. K. Despande, *Growth and branching of CuO nanowires by thermal oxidation of copper*, Journal of Crystal Growth, vol. 289, no. 2, 670–675, (2006).

[16]. J. Tauc, R. Grigorovici, and A. Vancu, *Optical properties and electronic structure of amorphous germanium*, Physica Status Solidi, vol. 15, 627–637, (1966).

[17]. S. K.Maji, N. Mukherjee, A. Mondal, B. Adhikary, and B. Karmakar, *Chemical synthesis of mesoporous CuO from a single precursor: structural, optical and electrical properties*, Journal of Solid State Chemistry, vol. 183, no. 8, 1900–1904, (2010).

[18]. D.Wu, Q. Zhang, and M. Tao, *LSDA+U study of cupric oxide: Electronic structure and native point defects*, Physical Review B—Condensed Matter and Materials Physics, vol. 73, no. 23, Article ID 235206, (2006).

[19]. M. Vila, C.Diaz-Guerra, and J. Piqueras, *Optical and magnetic properties of CuO nanowires grown by thermal oxidation*, Journal of Physics D-Applied Physics, vol. 43, no. 13, 135403– 135409, (2010).

[20]. C. Carel, M.Mouallem-Bahout, and J. Gaud´e, *Re-examination of the non-stoichiometry and defect structure of copper(II) oxide or tenorite, Cu1±ℰO or CuO1±ε: A short review*, Solid State Ionics, vol. 117, no. 1-2, 47–55, (1999).

[21]. Y. K. Jeong and G. M. Choi, *Nonstoichiometry and electrical conduction of CuO*, Journal of Physics and Chemistry of Solids, vol. 57, no. 1, 81–84, (1996).

[22]. A. Aslani, *Controlling the morphology and size of CuO nanostructures with synthesis by solvo/hydrothermal method without any additives*, Physical B: Condensed Matter, vol. 406, no. 2, 150–154, (2011).

[23]. K. Mageshwari and R. Sathyamoorthy, *Flower-shaped CuO nanostructures: synthesis, characterization and antimicrobial activity*, Journal of Materials Science & Technology, vol. 29, no. 10, 909–914, (2013).

[24]. B. A.Gizhevskiˇı,Y.P. Sukhorukov, A. S.Moskvinet al., *Anomalies in the optical properties of nanocrystalline copper oxides CuO and Cu2O near the fundamental absorption edge*, Journal of Experimental and Theoretical Physics, vol. 102, no. 2, 297– 302, (2006).

[25]. A. Aslani and V. Oroojpour, *CO gas sensing of CuO nanostructures, synthesized by an assisted solvothermal wet chemical route*, Physica B: Condensed Matter, vol. 406, no. 2, 144–149, (2011).

[26]. B. Toboonsung and P. Singjai, *Formation of CuOnanorods and their bundles by an electrochemical dissolution and deposition process*, Journal of Alloys and Compounds, vol. 509, no. 10, 4132–4137, (2011).

[27]. C. Jin, K. Baek, S. Park, H. W. Kim, W. I. Lee, and C. Lee, *Influence of SnO2 coating and thermal annealing on the structure and luminescence properties of CuO nanorods*, Solid State Communications, vol. 150, no. 37-38, 1812–1817, (2010).

[28]. S.-S. Chang, H.-J. Lee, and H. J. Park, *Photoluminescence properties of spark-processed CuO*, Ceramics International, vol. 31, no. 3, 411–415, (2005).

[29]. T.Kimura, Y. Sekio, H. Nakamura,T. Siegrist, andA.P.Ramirez, *Cupric oxide as an induced-multiferroic with high-TC*, Nature Materials, vol. 7, no. 4, 291–294, (2008).

[30]. V. Bisht, K. P. Rajeev, and S. Banerjee, *Anomalous magnetic behavior of CuO nanoparticles,* Solid State Communications, vol. 150, no. 17-18, 884–887, (2010).

[31] A.O. Adeyeye, G. Shimon, *in Handbook of Surface Science*, (2015)

[32]. Singh DP, Ali N. *Synthesis of TiO2 and CuO nanotubes and nanowires.* Science Advanced of Materials; 2:295–335 (2010).

[33]. Anandan S, Yang S. *Emergent methods to synthesize and characterize semiconductor CuO nanoparticles with various morphologies—an overview.* J Experiment Nanoscience; 2: 23–56 (2007).

[34]. Li Y, Yang XY, Feng Y, Yuan ZY, Su BL. *One-dimensional metal oxide nanotubes, nanowires, nanoribbons, and nanorods: synthesis, characterizations, properties and applications.* Crit Rev Solid State Material Science; 37:1–74, (2012).

[35]. Filipicˇ G, Cvelbar U. *Copper oxide nanowires: a review of growth.* Nanotechnology; 23:194001, (2012).

[36]. Liu Y, Chu Y, Zhuo Y, Li M, Li L, Dong L. *Anion-controlled construction of CuO honeycombs and flowerlike assemblies on copper foils.* Crystal Growth Design; 7:467–70, (2007).

[37]. Vaseem M, Umar A, Kim SH, Hahn Y-B. *Low-temperature synthesis of flower-shaped CuO nanostructures by solution process: formation mechanism and structural properties.* J Physical Chemistry C; 112:5729–35, (2008).

[38]. Zheng X, Xu C, Tomokiyo Y, Tanaka E, Yamada H, Soejima Y. *Observation of charge stripes in cupric oxide.* Physical Review Letter; 85:5170–5173, (2000).

[39]. MacDonald H. *Copper oxides get charged up*. Nature; 414:409–410, (2001).

[40]. Song M-K, Park S, Alamgir FM, Cho J, Liu M. *Nanostructured electrodes for lithium-ion and lithium-air batteries: the latest developments, challenges, and perspectives.* Material Science Engineering R Rep; 72:203–252, (2011).

[41]. Kislyuk VV, Dimitriev OP. *Nanorods and nanotubes for solar cells*. J Nanosci Nanotechnol; 8:131–148, (2008).

[42]. Choi KJ, Jang HW. *One-dimensional oxide nanostructures as gas-sensing materials: review and issues.* Sensors (Basel, Switzerland); 10:4083–4099, (2010).

[43]. Rahman MM, Saleh Ahammad aJ, Jin J-H, Ahn SJ, Lee J-J. *A comprehensive review of glucose biosensors based on nanostructured metal-oxides.* Sensors (Basel, Switzerland); 10:4855–4886, (2010).

[44]. Zhou LP, Wang BX, Peng XF, Du XZ, Yang YP. *On the specific heat capacity of CuO nanofluid*. Advaned Mechanism Engineering; 2010:1–4 (2010).

[45]. Wang SBB, Hsiao CHH, Chang SJJ, Lam KTT, Wen KHH, Hung SCC. *A CuO nanowire infrared photodetector*. Sensor Actuat A: Physics; 171:207–211, (2011).

[46]. Rossi C, Zhang K, Esteve D, Alphonse P, Tailhades P, Vahlas C. *Nanoenergetic materials for MEMS: a review*. J Microsystem and Systems; 16:919–931, (2007).

[47]. Zhu YW, Yu T, Cheong FC, Xu XJ, Lim CT, Tan VBC. *Large-scale synthesis and field emission properties of vertically oriented CuO nanowire films.* Nanotechnology; 16:88–92, (2005).

[48]. Zhang X, Shi W, Zhu J, Kharistal D, Zhao W, Lalia B. *High-power and high-energy-density flexible pseudocapacitor electrodes made from porous CuO nanobelts and single-walled carbon nanotubes.* ACS Nano; 5:2013–2019, (2011).

[49]. Ali I. *New generation adsorbents for water treatment.* Chemical Review; 112:5073–5091, (2012).

[50]. Yu X-Y, Xu R-X, Gao C, Luo T, Jia Y, Liu J-H, et al. *Novel 3D hierarchical cotton-candy-like CuO: surfactant-free solvothermal synthesis and application in As(III) removal.* ACS Applied Material Interfaces; 4:1954–1962, (2012).

[51]. Liu J, Jin J, Deng Z, Huang S-Z, Hu Z-Y, Wang L, et al. *Tailoring CuO nanostructures for enhanced photocatalytic property.* J Colloid Interface Sciennce; 384:1–9, (2012).

[52]. Kumar R, Diamant Y, Gedanken A. *Sonochemical synthesis and characterization of nanometer-size transition metal oxides from metal acetates.* Chem Mater; 12:2301–2305, (2000).

[53] Zhang X, Wang G, Liu X, Wu J, Li M, Gu J, et al. *Different CuO nanostructures: synthesis, characterization, and applications for glucose sensors.* J Physiscal Chemistry C; 112:16845–16849, (2008).

[54]. Vayssieres L, Rabenberg L and Manthiram A. '*Aqueous chemical route to ferromagnetic 3-D arrays of iron nanorods*. Nano letters; Vol. 2 No. 12, pp 1393-1395, (2002)

[55]. Spencer MJS. *Gas sensing applications of 1D-nanostructured zinc oxide: insights from density functional theory calculations*. Progress Materials Science; 57:437–486, (2012).

[56]. Sui R, Charpentier P, Domling A, Wang W, Wang K, Gonzalez-Gallardo S. *Synthesis of metal oxide nanostructures by direct sol–gel chemistry in supercritical fluids.* Chemistry Review; 112:3057–3082, (2012).

[57]. Xia Y, Yang P, Sun Y, Wu Y, Mayers B, Gates B. *One-dimensional nanostructures: synthesis, characterization, and applications.* Advanced Materials; 15:353–389, (2003).

[58]. Vayssieres L. *On the design of advanced metal oxide nanomaterials.* International Journal Nanotechnology; 1:1–41, (2004).

[59]. Wang ZL. *Zinc oxide nanostructures: growth, properties and applications.* Journal of Physics: Condense Matter; 16: R829–R858, (2004).

[60]. Shankar K, Basham JI, Allam NK, Varghese OK, Mor GK, Feng X. *Recent advances in the use of TiO2 nanotube and nanowire arrays for oxidative.* Journal of Physical Chemistry C; 113:6327–6359, (2009).

[61]. Teja AS, Koh P-Y. *Synthesis, properties, and applications of magnetic iron oxide nanoparticles.* Progress Crystal Growth Characterization of Materials; 55:22–45, (2009).

[62]. Pan J, Shen H, Mathur S. *One-dimensional SnO2 nanostructures: synthesis and applications*. Journal of Nanotechnology; 2012:1–12, (2012).

[63]. Jun Y-W, Choi J-S, Cheon J. *Shape control of semiconductor and metal oxide nanocrystals through nonhydrolytic colloidal routes*. Angew *Chemie - International Edition*, (English); 45:3414–3439, (2006).

[64]. Cao M, Hu C, Wang Y, Guo Y, Guo C, Wang E. *A controllable synthetic route to Cu, Cu2O, and CuO nanotubes and nanorods.* Chemistry, Engineering (Cambridge); 1:1884–1885, (2003).

[65]. Cheng G. *Synthesis and characterisation of CuO nanorods via a hydrothermal method.* Micro Nano Letters; 6:774, (2011)

[66]. Gao X, Bao J, Pan G, Zhu H, Huang P, Wu F. *Preparation and electrochemical performance of polycrystalline and single crystalline CuO nanorods as anode materials for Li ion battery.* Journal of Physical Chemistry B; 108:5547–5551, (2004).

[67]. Dar Ma, Kim YS, Kim WB, Sohn JM, Shin HS. *Structural and magnetic properties of CuO nanoneedles synthesized by hydrothermal method.* Applied Surface Science; 254:7477–7481, (2008).

[68]. Zhang Q, Zhang K, Xu D, Yang G, Huang H, Nie F, Liu C, Yang S. *CuO nanostructures: Synthesis, characterization, growth mechanisms, fundamental properties, and applications*; Progress in Materials Science 60 208–337, (2014)

[69]. G. F. Fine, L. M. Cavanagh, A. Afonja, R. Binions, Sensors 10, 5469, (2010).

[70]. X. Wang, S. S. Yee, W. P. Carey, **Sens**. **Actuators**. B 24-25, 454, (1995).

[71]. C. Yang, F. Xiao, J. Wang, X. Su. *3D flower- and 2D sheet-like CuO nanostructures: Microwave-assisted synthesis and application in gas sensors.* Sensors and Actuators B 207, 177–185, (2015).

[72]. N. Zhang, S. Ruan, J. Han, Y. Yin, X. Li, C. Liu, S. Adimi, S. Wen, Y. Xu, *Oxygen vacancies dominated CuO@$ZnFe_2O_4$ yolk-shell microspheres for robust and selective detection of xylene*, Sensors and Actuators: B 295, 117-126, (2019).

[73]. H. Gao, J. GuO, Y. Li, C. Xie, X. Li, L. Liu, Y. Chen, P. Sun, F. Liu, X. Yan, F. Liu, G. Lu. *Highly selective and sensitive xylene gas sensor fabricated from NiO/$NiCr_2O_4$ p-p nanoparticles.* Sensors & Actuators: B. Chemical 284, 305-315, (2019).

[74]. I Kortidis, H C. Swart, S Sinha Ray, D E. Motaung. *Detailed understanding on the relation of various pH and synthesis reaction times towards a prominent low temperature H_2S gas sensor based on ZnO nanoplatelets.* Results in Physics 12, 2189-2201, (2019).

[75]. B. Zhang, F. Qu, X. Zhou, S. Zhang, T. Thomas, M. Yang. *Porous coral-like $NiCo_2O_4$ nanospheres with promising xylene gas sensing properties.* Sensors & Actuators B 261, 203-209, (2018).

[76]. J.-H. Kim, H.-M. Jeong, C.W. Na, J.-W. Yoon, F. Abdel-Hady, A.A. Wazzan, J.-H. Lee. *Highly selective and sensitive xylene sensors using Cr_2O_3-$ZnCr_2O_4$ hetero-nanostructures prepared by galvanic replacement.* Sensors & Actuators B 235, 498-506, (2016).

[77]. I. Kortidis, S. Lushozi, N. Leshabane, S. S. Nkosi, O. M. Ndwandwe, J. Tshilongo, N. Ntsasa, D. E. Motaung. *Selective detection of propanol vapour at low operating temperature utilizing ZnO nanostructures.* Ceramics International 45, 16417-16423, (2019).

[78]. F. Li, S. Ruan, N. Zhang, Y. Yin, S. Guo, Y. Chen, H. Zhang, C. Li. *Synthesis and characterization of Cr-doped WO_3 nanofibers for conductometric sensors with high xylene sensitivity.* Sensors and Actuators B 265, 355–364, (2018).

[79]. F. Li, S. Guo, J. Shen, L. Shen, D. Sun, B. Wang, Y. Chen, S. Ruan. *Xylene gas sensor based on Au-loaded $WO_3 \cdot H_2O$ nanocubes with enhanced sensing performance.* Sensors and Actuators B 238, 364–373, (2017).

[80]. H. Gao, D. Wei, P. Lin, C. Liu, P. Sun, K. Shimanoe, N. Yamazoe, G. Lu. *The design of excellent xylene gas sensor using Sn-doped NiO hierarchical nanostructure.* Sensors and Actuators B 253, 1152–1162, (2017).

[81]. O. K. Varghese, D. W. Gong, M. Paulose, K. G. Ong and C. A. Grimes, "*Hydrogen sensing using titania nanotubes*" Sensors Actuators B., Vol. 93, pp. 338-344, (2003).

CHAPTER IV

4.1. Characterization of the as-synthesized CuO samples.

After the samples have been successfully synthesized, they were then subjected to various characterization techniques detailed in chapter 3. The phase structures of these powders were characterised by X-ray diffraction (XRD) using a Bruker Advance D8 instrument, with a scan rate of 0.3° per minute. Images of the surface morphology and particle size of the powders were captured using a scanning electron microscope (SEM, Carl ZEISS Sigma VP-03-67). High-resolution transmission electron microscope (HR-TEM) images were recorded using a JEOL 1400 system. The PL spectra of the samples were excited at room temperature with a continuous He-Cd laser, using a wavelength of 325 nm (3.82 eV) chopped at 120 Hz and collected using a Horiba iHR320 spectrometer with entrance and exit slits set to 250 μm and a photomultiplier tube detector (R9943-02) operating at 1300 V, linked to a lock-in amplifier. An PHI 5400 Versaprobe x-ray photoelectron spectroscopy (XPS) system was used to examine the oxidation state of the samples with a monochromatic Al Kα (1486.7 eV) X-rays at a pressure of less than 10^{-8} mbar. N_2 adsorption-desorption isotherms and Brunauer-Emmett-Teller (BET) surface area studies were performed using a Micromeritics TRISTAR 3020 surface area analyser.

4.2. Structural and morphological properties of of Zn doped CuO and undoped CuO nanostructure

Figure 4.1a illustrates XRD patterns of pure CuO and Zn doped CuO (0.1, 0.25, 0.50, 1.0 and 2.0 at. %) nanoplatelets. The diffraction peaks coincide well with the standard data of pure CuO (JCPDs file no.: 41-0254/0706). This high quality crystalline CuO has a monoclinic structure with space group C2/c. Broadening of the diffraction peaks can be ascribed to the nano-sizing of the crystals. The shifting of the two peaks for the -111 and 111 planes to higher and back to lower angles (see figure 4.1.b) suggest a structural deformation, due to the addition of Zn^{2+} into the CuO matrix. By increasing the Zn^{2+} (i.e. 0.25 and 0.50 at. %) in the CuO matrix, the formation of a secondary phase prominent at 2θ = 26° and 37° was observed. This phase could be attributed to $Cu(OH)_2$. Figure 1c and d demonstrate the crystallite sizes and lattice strains calculated using the William-Hall (W-H) method **[2]**. The crystallite size decreased drastically when the Zn concentration exceeds 0.5 at. %, while the lattice strain increased.

Figure 4.2 depicts the morphologies of the CuO and Zn doped CuO nanostructures. **Figure 2a** displays the pure CuO exhibiting nanostructures.Upon doping with 0.1 at. % Zn, the diameter of the nanoplatelets reduced, while their surface became smoother (see **Figure 4.2b**). A slight increased the diameter of the nanoplatelets is observed when the doping concentration increases from 0.25 at. % to 2.0 at. % see **Figure 4.2c-f**. Such an increase, more especially at 2.0 at. %, is probably due to a change of morphology with bigger diameters.

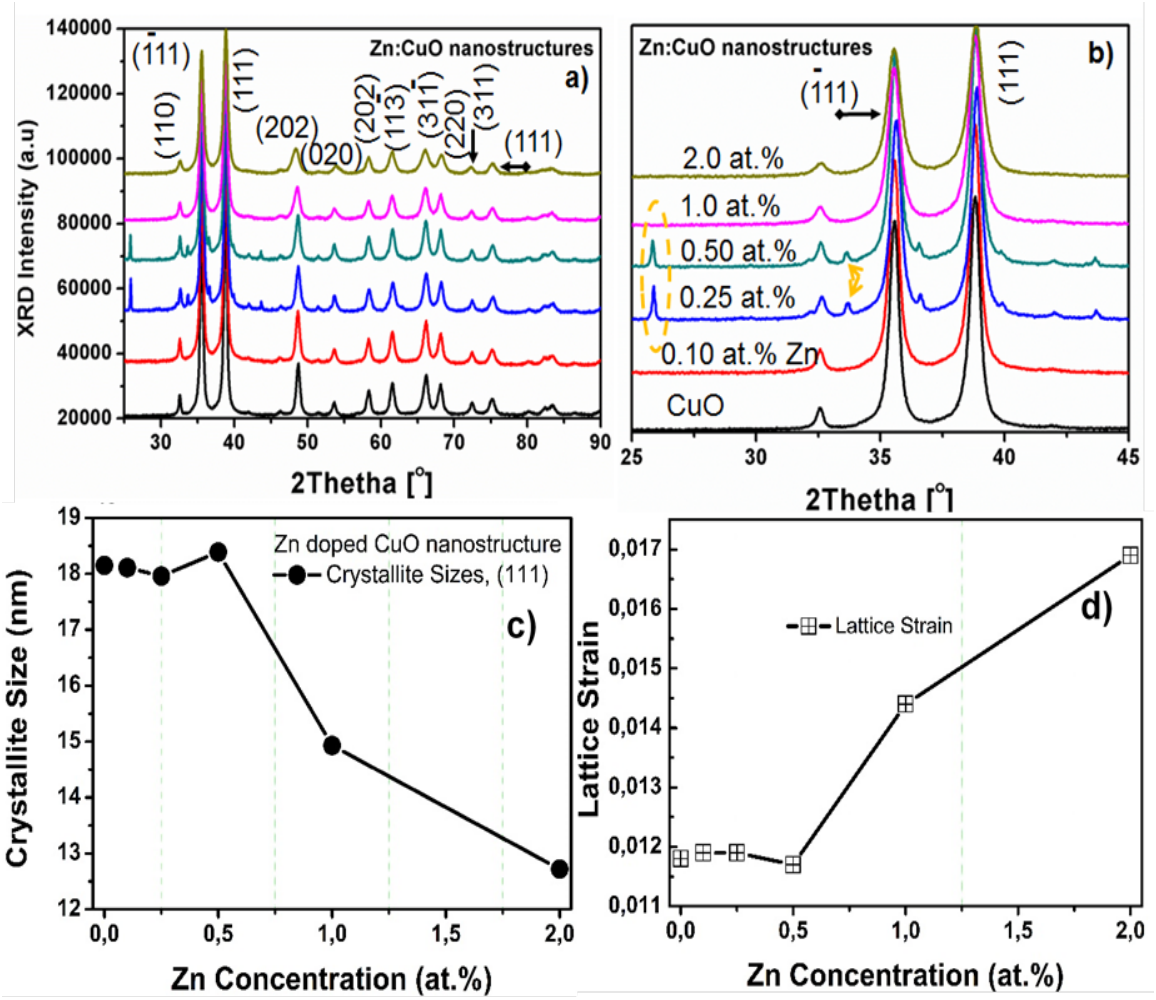

Figure 4. 1*. X-ray diffraction patterns of CuO and Zn doped CuO nanoplatelets. a) wide scan and b) narrow scan showing the prominent -111 and 111 peak reflections, c) effect of Zn doping on the crystallite size and d) lattice strain.*

Elemental mapping for CuO and 0.1 at. % Zn doped CuO (**Figure S3** of the Supplementary Information file in Appendix A (SI)) showed a homogenous distribution of all the elements. High resolution-transmission electron microscopy (HR-TEM) and selected area electron diffraction (SAED) patterns were used to investigate the internal structural information and crystalline behaviour of the Zn doped CuO nanoplatelets and are given in **Figure 4.3** which shows that they are polycrystalline in nature. **Figure 4.3a**

exhibits CuO lattice fringes with a *d*-spacing of 0.30 nm and 0.25 nm corresponding to the (110) and (111) planes, respectively. The inset of **Figure 4.3a** shows the SAED pattern of the CuO confirming its polycrystalline behaviour.

4.3. Gas sensing properties of Zn doped CuO and undoped CuO nanoplatelets based sensors

Gas sensing properties of pure and Zn doped CuO nanoplatelets were examined at different operating temperatures ranging from room temperature (25 °C) up to a maximum of 150°C to avoid any permanent structural change. These samples had been annealed at 200°C during synthesis. The sensors were exposed to toluene, xylene, benzene, ethanol, propanol, ethylene, ammonia, hydrogen and liquefied petroleum gas (LPG). Superior selectivity is one of the critical necessities as gas sensors as to elude interference from the other gases during sensing. To investigate the selectivity of various Zn doped CuO nanoplatelets, the sensing layers were exposed to various gases at 100 ppm and at an optimal operating temperature of 150 °C, at a bias voltage of 2 V.

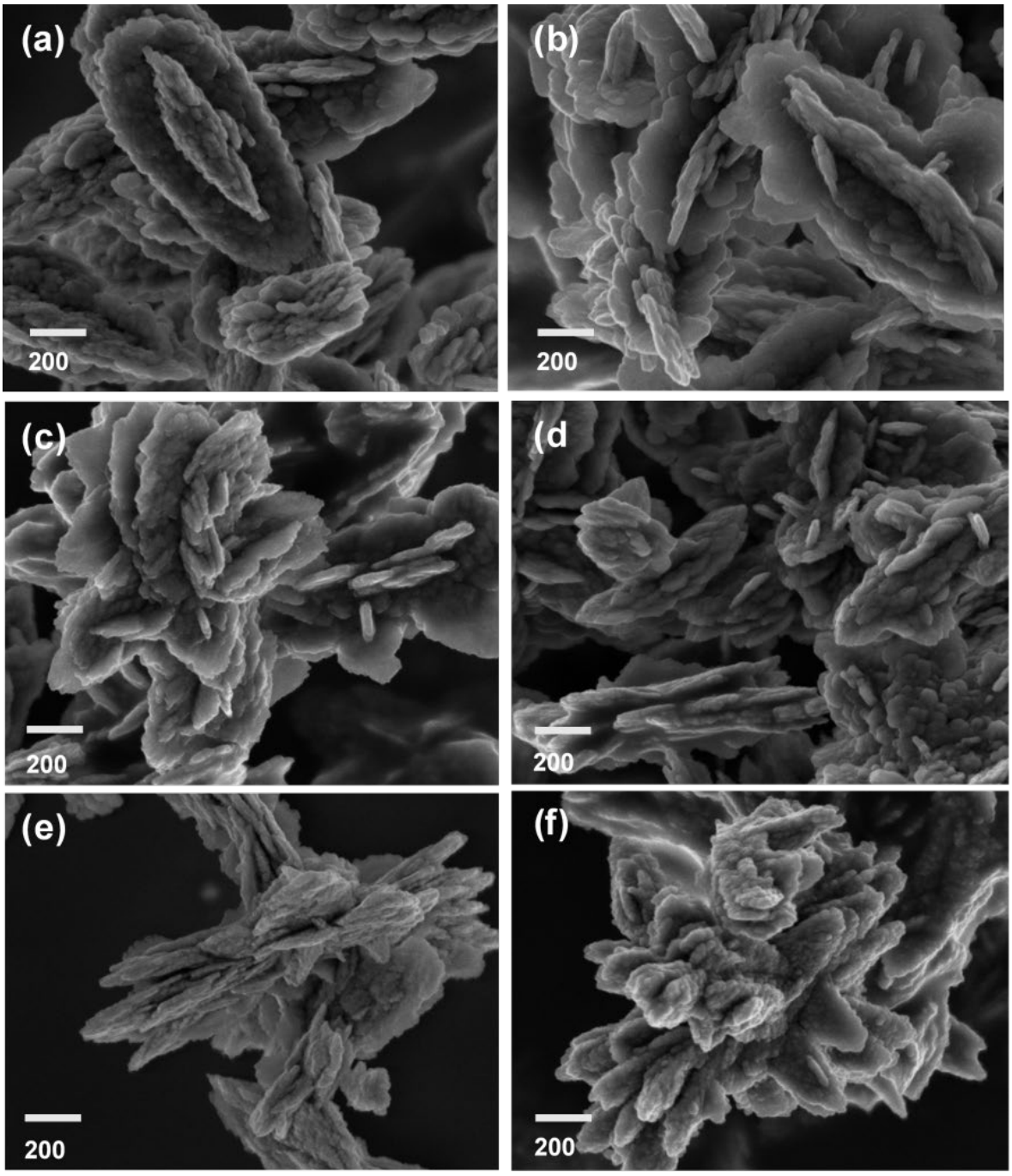

Figure 4. 2. *The Scanning electron microscopy images of a) pure CuO, and Zn doped CuO b) 0.1 at. %, c) 0.25 at. %, d) 0.50 at. %, e) 1.0 at. %, f) 2.0 at. %.*

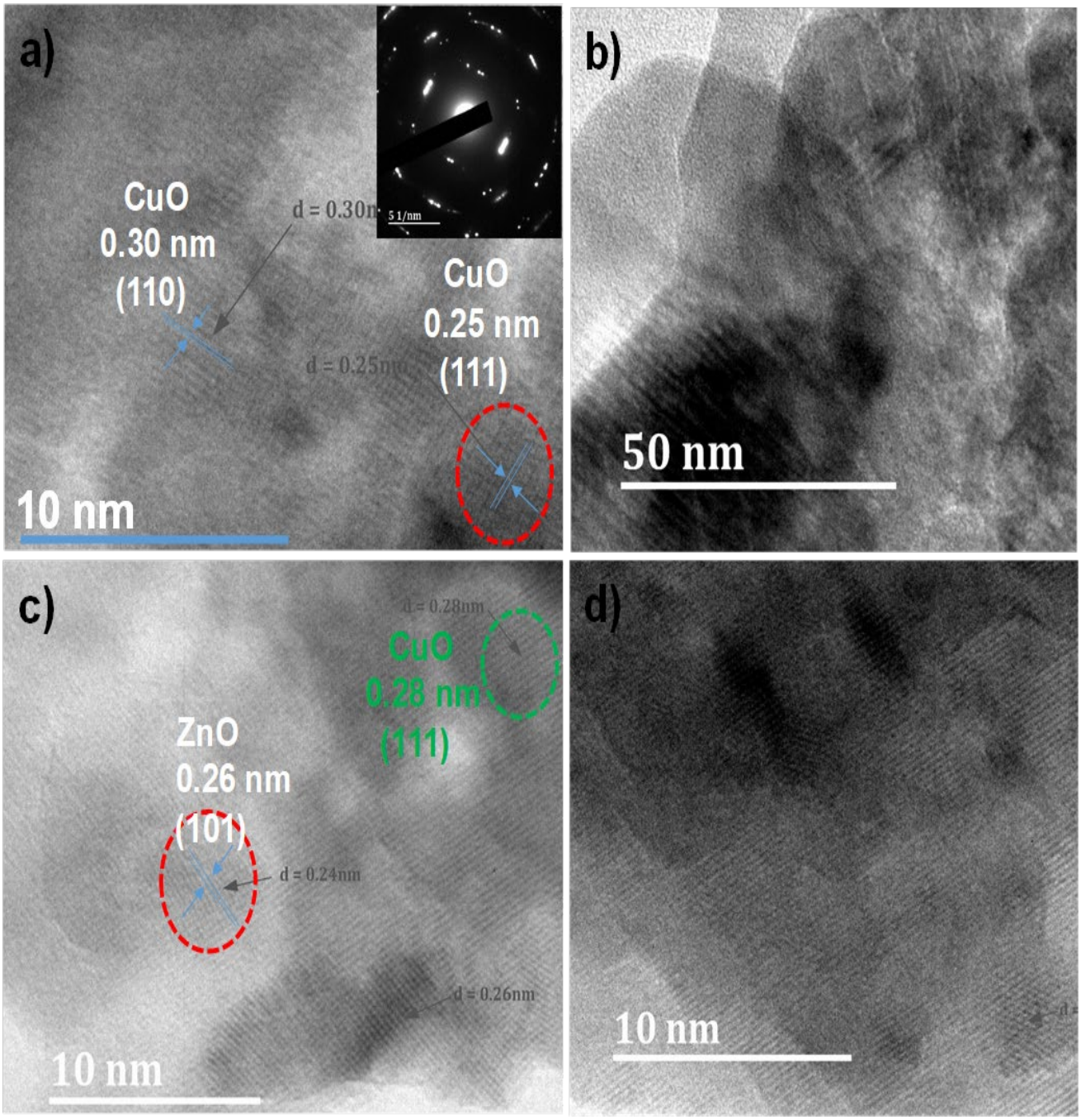

Figure 4. 3. *The Typical HRTEM images of the (a) pure CuO, (b) 0.1 at. % Zn, (c) 0.25 at. % Zn and (d) 0.50 at. % Zn nanoplatelets*

Figure 4.4a presents the selectivity histogram. Based on the attained findings, the two sensing materials, pure CuO and 0.1at. % Zn doped CuO, showed a drastic increase in

gas response at 100 ppm xylene in comparison to other gases. The maximum response of these two sensors was 42.71 and 53.10, respectively, which is about 6 times higher than other interfering gases. The higher selectivity of the two sensors towards xylene is probably due to the dissociation energy for xylene, which is much lower (281 kJ/mol) compared to the other interference gases. Furthermore, xylene generally possesses enhanced active chemical properties, in comparison to benzene and toluene, due to an extra methyl group in the benzene ring **[3]**. A radar plot to represent each gas (with the exception of LPG since a minimum concentration used was 1000 ppm) for both pure CuO and 0.1at. % Zn:CuO is shown in **Figure 4.4b**. The shaded-area represents the gas response and it is clear that xylene exhibited the highest response for both these sensors at 150 °C, followed by ethanol. When looking at the areas of both sensors, the pure CuO area is greater than that of the 0.1 at. % Zn:CuO. A sensor with greater area-spread in the radar plot is unfavourable on the selectivity, so the 0.1 at. % Zn:CuO based-sensor was more selective compared to the pure CuO sensor.

The other important factor is the ability of a sensor to respond to a target gas (xylene) in the presence of other interfering gases. That factor, call it β, can be calculated using the response ratios between the target gas and interfering gases. A higher β would mean a sensor has a great selectivity to discriminate the target gases. Comparing β for the target gas (xylene) to ethanol and liquefied petroleum gas (LPG), it is evident that the sensor (0.1 at. % Zn:CuO) exhibited higher response than ethanol, $\beta_{X/Eth}$ = 6.72. Similarly, the pure CuO exhibited higher response than LPG, $\beta_{X/LPG}$ = 3.97. Ethanol has the higher response in the interfering gases than any of the other gases.

The working temperature, doping and the gas concentration significantly influence the sensing. To explore the optimal working temperature and ideal dopant concentration the responses of various doped Zn:CuO samples were tested for different operating temperatures at 100 ppm xylene vapour. As indicated in **Figure 4c**, the response of the sensors increased with increasing the operating temperature. More specifically, the pure CuO and 0.1 at. % Zn:CuO showed a significant increase of gas responses between 100 and 150 °C of 42.71 and 53.10, respectively. The pure CuO also showed an improved response, although slightly less than that of 0.1 at. % Zn. **Figure 4.4d** shows the dynamic response curves of the gas sensor to xylene with different gas concentrations at 150°C. The sensor's resistance increased slowly with the xylene gas injection and also recovered slowly from xylene to air. The sensor's resistance almost tripled to 8.0×10^3 kΩ for 100 ppm xylene gas. It is worth mentioning that the response values for both pure CuO and 0.1 at. % Zn:CuO were much higher than their counterpart samples over the interfering gases and xylene concentration range. There is one challenging behaviour for the xylene sensing response observed in **Figure 4.4e**. Most sensors turn to follow a linear relationship between response and gas concentration. This relationship is often fitted with a linear fit regression to extract sensor parameters such as slope and detection limit. In the current case the sensor's response to xylene seems to present regional linear fits to various concentrations of xylene, the sub-ppm region, intermediate ppm region and high ppm region.

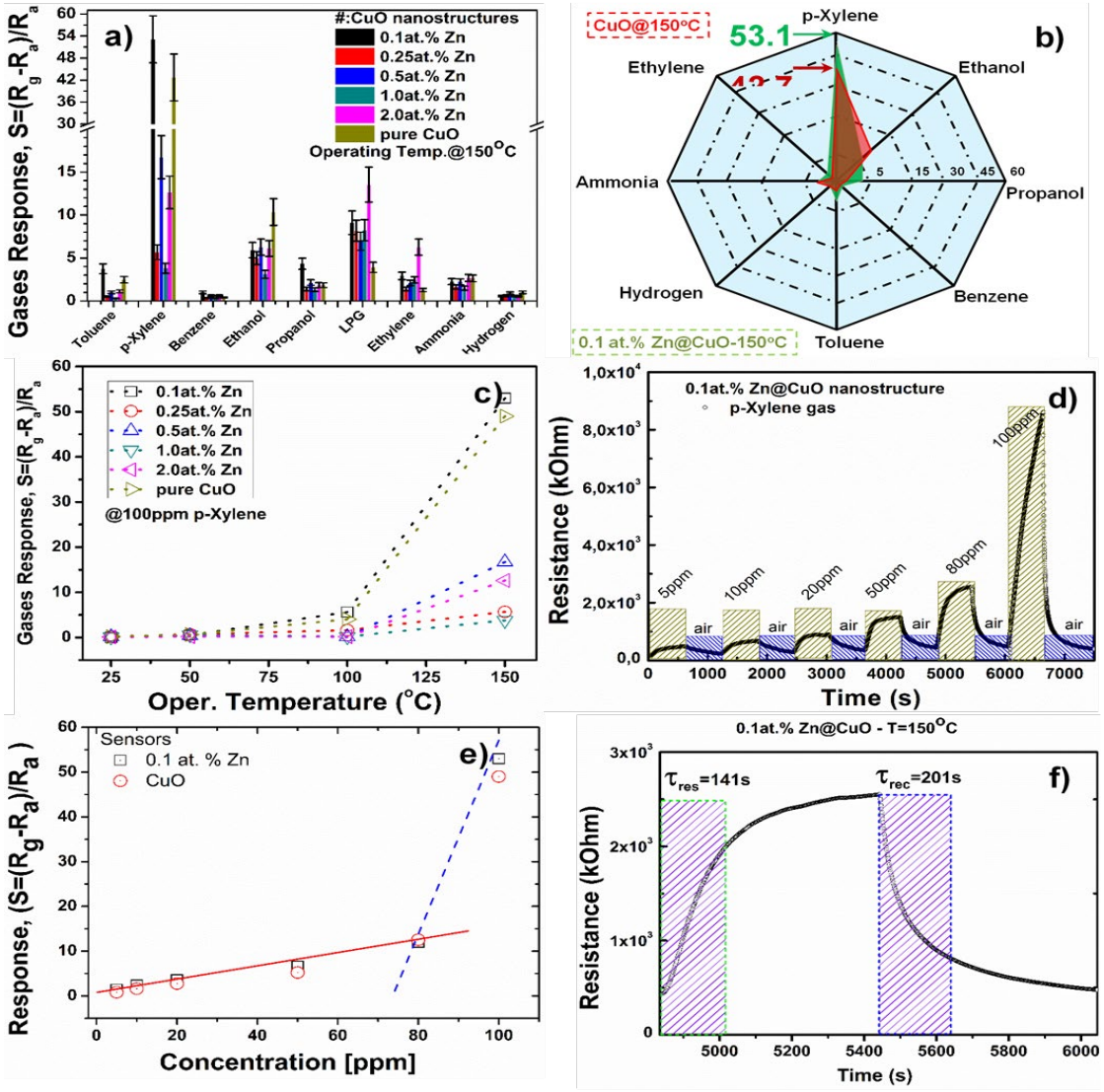

Figure 4. 4. *(a) Selectivity histogram of nine different gases at 100 ppm concentrations at 150 °C and responses. (b) Radar plot of the different gases and their respective responses at 150 °C. (c) p-Xylene gas at 100 ppm at different operating temperatures.*

This type of behaviour is also evident in other reports, but not mentioned and discussed **[4-7]**. Arguable, one can fit a Boltzmann function, in the equation below to this data, where A_1, A_0, x, x_0, Δx are the sensor's constants.

$$f \to \frac{A_1 + (A_1 - A_0)}{\left[1 + e^{(x-x_0)/\Delta x}\right]} \tag{4.1}$$

The constant parameter Δ*x* would represent a slope in this case, for both regions, low and high. Although the 5 ppm of p-xylene vapour was the lowest concentration conducted experimentally in the current study, the theoretical detection limits (signal to-noise ratio >3) derived from this formula $D_L = 3(^{RMS_{noise}}/_{Slope})$ **[7, 8]** were estimated to be 0,21 and 0,11 ppm for pure CuO and 0.1 at. % Zn doped CuO, respectively. Note, the RMS noise is the root-mean-square-deviation extracted from the sensor's response before any gas analyte was injected. This ppb level (i.e. 110 ppb) detection limit for 0.1 at. % Zn doped CuO validates its potential use in high performance VOC sensors. **Figure 4.4f** shows the response and recovery times of 141 s and 201 s for the undoped and doped samples, respectively, for 100 ppm xylene. Since the applied bias voltage directly influences the sensing properties, we carried out the sensing response at three different bias voltages, i.e. 0.1, 1 and 2 V.

The sensing characteristics of the optimized 0.1 at. % Zn:CuO sensor investigated at different applied bias voltages as shown **Figure 4.5**. **Figure 4.5a** displays the sensor resistance in air (R_a) and response plots versus the applied voltage of the optimized 0.1 at. % Zn: CuO sensor to 100 ppm xylene at an applied bias of 0.1–2 V. It is clear that at low voltage bias the sensor shows a small R_a value of 528 × 10^2 kΩ, while increasing the voltage to 0.5 V the maximum R_a value of 626 × 10^2 kΩ is observed, which decreased to 570 × 10^2 kΩ at 2 V. The response increased with an increase in applied bias, showing a maximum response of 53 at 2 V. Such an increase in response with the

applied bias could be due to the decreased conduction electrons. Kim et al. **[9]** observed similar behaviour where the response of both Pt- and Pd functionalized ZnO nanowire based sensors increased with applied voltage.

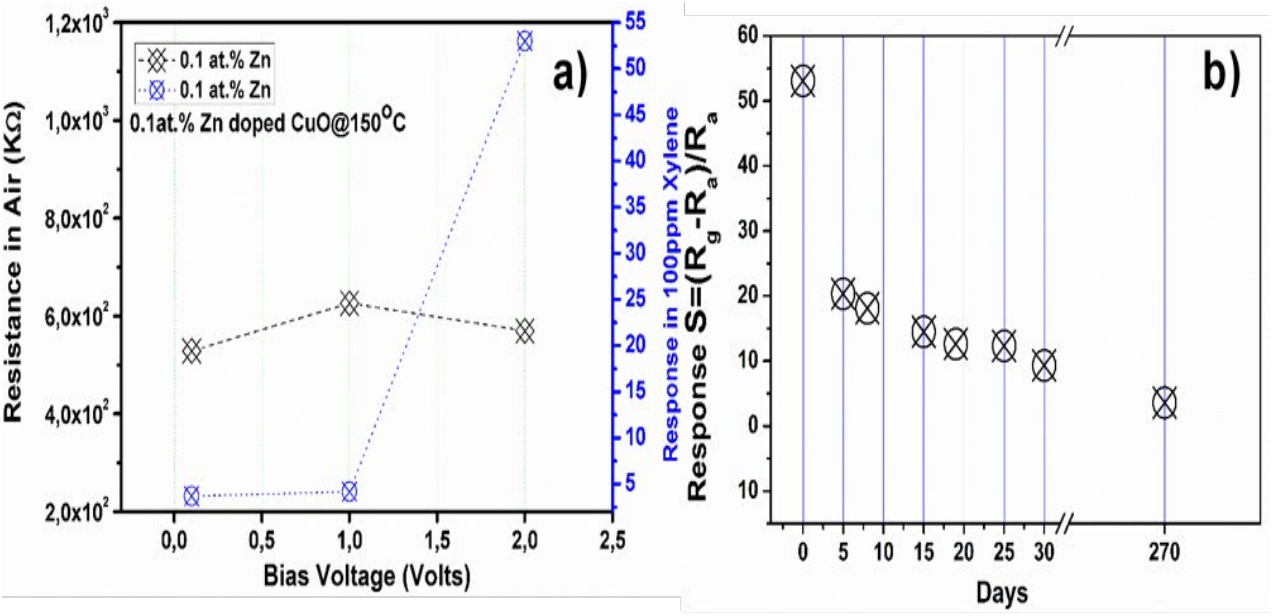

Figure 4. 5. *(a) Response and resistance curves of the 0.1 at. % Zn doped CuO to pulse of 100 ppm xylene and in air as function of applied voltage of 0.1 V, 1 V and 2 V. (b) Stability test measurement to pulses of 100 ppm xylene over many days.*

The Long-term stability is also an important parameter for practical application in gas sensing. To test this the best performing sensors (i.e. pure CuO and 0.1 at. % Zn doped CuO) were stored under ambient conditions for 9 months and afterwards further exposed to 100 ppm xylene at 150 °C under the applied voltage of 2 V. As shown in **Figure 4.5b**, though the response of the 0.1 at. % Zn doped CuO reduced by 60% after 5 days, nonetheless, 270 days later the response remained stable in comparison to that of 5 days, showing an acceptable drift of 20%. Thus, we can conclude that the 0.1 at. % Zn doped CuO has a potential to demonstrate better gas sensing characteristics

towards xylene considering its rapid response−recovery times, good response, low detection limit, admirable selectivity, and possible operative stability. This sensor demonstrated reliable responses on humidity and reproducibility measurements as shown in the Appendix A in the ESI file (see **Figure S1b**).

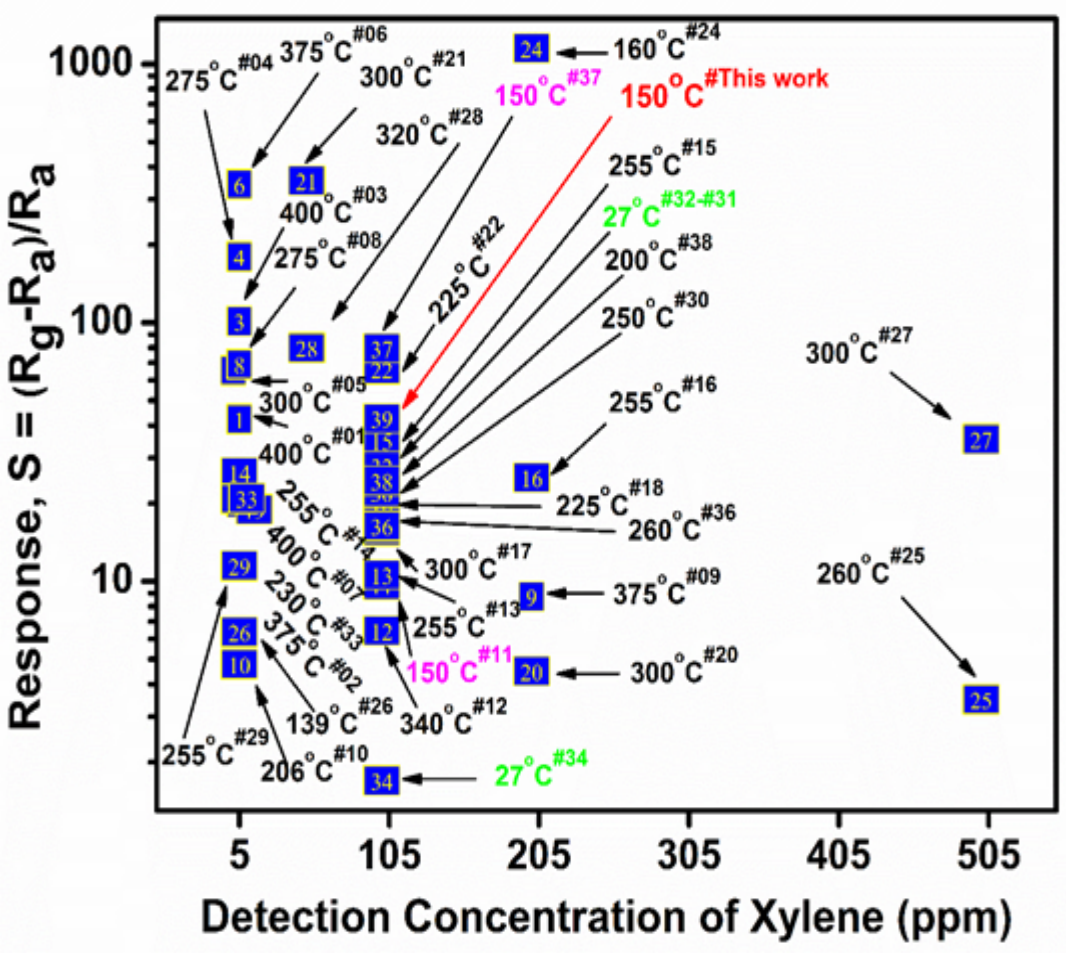

Figure 4. 6. *Graphical gas sensing mapping characteristics and comparison of different sensing materials to p-xylene vapors on various literature results and at the present study. Note: Numbers highlighted in blue and hashtag refer to references. All these references are archived in the ESI file and some are used within the thesis referenced accordingly.*

Figure 4.6 shows a comparison plot of all the sensors' responses in the open literature for xylene gas sensing at different concentrations and operating temperatures. The numbers highlighted in blue and hashtag refer to the references used and are all archived in the ESI file (Appendix A). Some are used within the article and referenced accordingly. Both sensors (CuO and 0.1 at. % Zn:CuO) showed responses a little above 42 and 53 at a 150 °C operating temperature against 100 ppm of xylene, respectively. From the literature survey, there is only one report of xylene gas at 150 °C operating temperature depicting low response of about 10.

This literature survey mapping in **Figure 4.6** contains only three reports at this operating temperature and the target gas concentration including this current work. There is a high xylene response reported at 160 °C of over 1000; however, the concentration was 205 ppm. It is noteworthy to mention that we are not aware of other reports on pure CuO and Zn doped CuO for xylene gas sensing. Zhang et al. **[4]** reported on xylene sensing using $ZnFe_2O_4$ yolk-shell ferrites at an operating temperature of 225 °C. Their response was only limited to 24 with the incorporation of CuO as a catalyst for the oxidation of xylene due to the increase of the absorbed oxygen vacancies. Many of these reports in Figure 6a demonstrated high response at high operating temperatures. The surface morphology and nano-scaling seem to be the main contributors to high performance towards p-xylene gas. Similar nano-platelet morphology for all the samples containing small traces of oxygen vacancies is exhibited with highly sensitivity and selectivity at relatively low Zn doping concentration and operating temperature.

4.4. Gas sensing mechanism of Zn doped CuO and undoped CuO nanostructures

The gas sensing phenomenon is discussed in detail in chapter 3. The crystallite size for CuO and 0.1 at. % Zn doped CuO were calculated to be about 18 nm for both sensors. As the Zn doping increased, the crystallite size reduced to about 12 nm and sensing performance drastically dropped. This is contrary to the sensing theory proposed elsewhere that reducing the particle size give rise to sensitivity **[7, 8]**. The earlier reactions describe the different oxygen ionization-taking place at various temperatures. In our case the enhanced sensing took place at 150 °C, and the following reaction describes (eqns 4.2 & 4.3) the possible interaction between the adsorbed ionic molecular oxygen and the xylene gas **[10]**:

$$\left(C_6H_4CH_3CH_3\right)_{gas} \xleftrightarrow{O^-} \left(C_6H_4CH_3CH_3\right)_{ads} \tag{4.2}$$

$$\left(C_6H_4CH_3CH_3\right)_{ads} + 21O^- \xrightarrow{@150^\circ C} 8CO_2 + 5H_2O_{(gas)} + 21e^- \tag{4.3}$$

Equation (4.3) demonstrates that CO_2, H_2O moisture and electrons are released during the oxidation process of the gas analyte. These electrons neutralise the holes in the conduction layer, thereby decreasing the resistance of the sensor during recovery. The introduction of Zn at higher concentrations of more than 0.1 at. % in this study resulted into a reduced sensing performances and such behaviour is explained in detail using the XPS and PL studies in the next sections.

4.5. Optical Properties of Zn doped CuO and undoped CuO nanoplatelets

The PL, analyses were carried out to support the gas sensing findings. **Figure 4.7a** shows the room temperature PL spectra of the pure CuO and that doped with various

concentrations of Zn. Doped samples exhibited an improved PL intensity of the nanoplatelets compared to pure CuO. The PL intensities of both the 0.1 at. % and 0.25 at. % Zn doped CuO were much higher and broader (i.e. 400-500 nm) than the rest of the samples. Meanwhile, the 0.50 at. % and 2.0 at. % Zn doped samples exhibited intermediate PL intensities. Both the pure CuO and 1.0 at. % Zn doped CuO exhibited the lowest PL intensities due to poor charge separations **[11, 12]**. Only the PL emission of the pure CuO was red-shifted with its peak around 450 nm. The broadness of emission in the visible spectrum range is normally due to oxygen vacancies and extrinsic defects from doping **[13]**. Oxygen vacancies are the prime intrinsic/native defects emanating from a lack of lattice oxygen or oxygen deficient regions in the metal oxide surface. They play a crucial role in the metal oxide functions.

They act as shallow donors. The near band edge UV emission spectra as indicated by an arrow in the pure CuO was suppressed (see **Figure 4.7a**). The origin of the UV emission in CuO is due to the recombination of electron hole pairs in free excitons **[13]**. More interestingly, **Figure 4.7b** shows the same PL spectra analysed in-situ at 150°C for both the pure CuO and 0.1 at. % of Zn doped CuO. It should point out that these samples showed the best sensing characteristics towards xylene gas at the same operating temperature of 150 °C. Interestingly, the emission peak of the 0.1 at. % Zn:CuO sample measured at 150 °C became much broader, extending from the UV up to the far visible range of the electromagnetic spectrum. Five peaks positioned at 3.53 eV (352 nm), 3.02 eV (411 nm), 2.49 eV (499 nm), 2.34 eV (531 nm) and 1.97 eV (631 nm) were obtained when deconvoluting the spectrum using Lorentzian/Gaussian fits (*see also in Appendix A, **Figure S2e***). According to Chand et al. **[14]** the UV emissions

centred at 359 and 383 nm are related to the band edge emissions of CuO, while the emission located at 411 nm is associated with CuO characteristics. The blue emission peak around 499 nm is linked to defect related emission or surface impurities like intrinsic defects, oxygen vacancies, oxygen interstitials and metal ions in CuO **[15]**. CuO is fundamentally p-type because of the presence of Cu vacancies. Hence, the radiative recombination flanked by donor level and acceptor level defect centres produces the noticed CuO emission peak. The green emission band positioned at 542 nm is ascribed to singly ionized oxygen vacancies **[15]**, while that at 2.29 eV (631 nm) could be linked to oxygen interstitials.

However, the pure CuO emission peaks were completely suppressed once the temperature was elevated to 150°C. Only a very low intensity PL peak is shown in appendix A figure S2c of the ESI file for the pure CuO, displaying emission in the range of 350-750 nm associated with point defects such as V_O and Cu vacancies. In addition, a PL emission stability behaviour of the pure CuO was performed. **Figure S2b** (as presented in Appendix A) of the ESI file shows that each time the PL measurements were repeated at room-temperature (few minutes' interval) the PL intensity decreased for the pure CuO. On the other hand, the systematic study of the elevation temperature interval of the pure CuO as shown the appendix A of **Figure S2a** (in the SI) demonstrates that the emission peak intensities significantly decreased. This further shows that the defects of the pure CuO sample were easily eliminated due to thermal effects. Meanwhile, the 0.1 at. % Zn:CuO sample showed systematic increase of broadness of the emission peak (**Figure S2d** of the ESI as seen in Appendix A), denoting its emission stability. Therefore, it can be concluded that the 0.1 at. % Zn:CuO

sample carry a relative higher localized concentration of structural defects i.e. oxygen vacancies and oxygen interstitials which were activated at higher temperatures, confirming higher sensing response as observed in **Figure 4.4**.

Our analysis indicates that the incorporation of Zn into CuO increased the number of localized oxygen vacancies, which are activated at elevated temperatures and confirmed to favour the oxygen adsorption, which further reacts with xylene to produce the large sensing resistance of the 0.1 at. % Zn:CuO based sensor. This is due to the fact that at room temperature the 0.1 at. % Zn:CuO based sensor showed very low response, and this was consistent with the PL analyses carried out at room temperature only showing low relative concentration of points defects. The response of 0.1 at. % Zn may be related to higher relative concentration of point defects observed at 150 °C, although the reason behind the higher response observed for pure CuO remained unknown since its PL intensity is quenched and suppressed at higher temperature (150 °C).

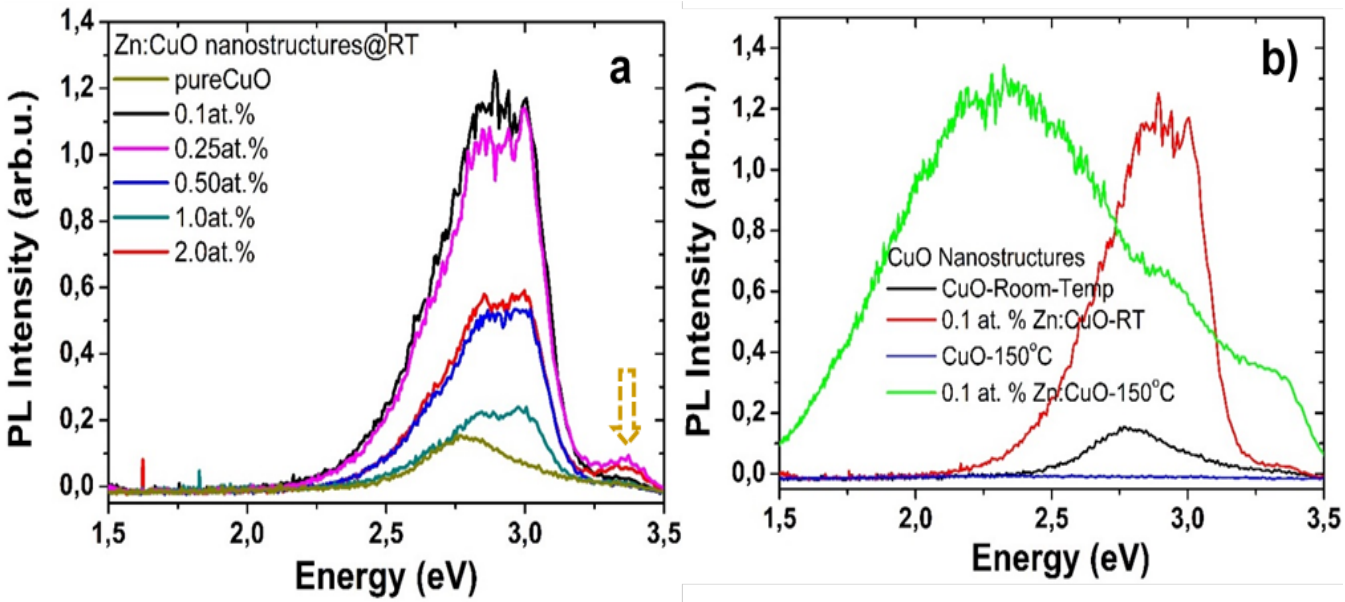

temperature and 150 °C.

4.6. Chemical composition and oxidation state of Zn doped CuO and undoped CuO nanostructures

The surface chemical composition was investigated for the pure and Zn doped CuO with various concentrations by XPS and the results of the O 1s core level peaks are shown in **Figure 4.8**. The survey spectrum shown in the *Appendix A* ESI file of **Figure S4** confirmed the presence of Cu and O on the surface. The wide scan survey shows a C 1s line (284.8 eV) which was used to calibrate the binding energies and for reference. The C peak was due to adventitious C due to handling and atmospheric exposure.

The asymmetric O 1s curves shown in **Figure 4.8** can be fitted by three peaks to represent the main oxygen components. The peaks positioned at 529.0 (O_i), 530.1 (O_{ii}) and 531.8 eV (O_{iii}) are assigned to lattice oxygen, O^{2-} in CuO (529.0 eV), oxygen deficient regions and/or chemisorbed species (530.1 eV) and hydroxides (531.8 eV) **[16]**. The peak area of the oxygen vacancies and interstitial occupy a significantly small portions. The area percentage of less than 10 corresponds to the hydroxides group. The oxygen vacancies are well known as electrons reservoirs from the conduction band to form an abundant number of adsorbed oxygen ions, resulting in an increased electron depletion layer on the surface of the sensor **[4, 7, 8, 11, 12]** and thus improving the gas sensing performance of a sensor. The XPS analysis are in agreement with the PL analyses as there are no oxygen defect related emissions (oxygen vacancies and interstitials). The Cu $2p_{3/2}$ and Cu $2p_{1/2}$ peaks (shown in **Figure S6** of the ESI in Appendix A) were found at 933.2 and 953.2 eV, respectively, accompanied by two distinct satellite peaks.

This indicates the Cu ions were in the +2 oxidation state **[10, 15, 16]**. The N_2 adsorption-desorption and BET analyses were conducted in order to investigate their possible contribution on the gas sensing. Usually, a variation in the morphology has effects on the pore distribution and the sensing performance. However, in **Figure 4.9** it is clear that the only variation on the pore size was observed for the CuO, showing the pore size of 11.22 nm in comparison to that of 10.43 nm for 0.1 at. % Zn doped CuO. With increased doping concentration the pore size distribution remained almost the same and there was no significant change in the morphology observed.

It is clearly observed that the doping does not affect the pore diameter, only changes are observed on the surface area, which increases with doping. The pure CuO showed a surface area of 21, 00 m^2/g, after doping with 2.0 at. %, it increased to 26, 64 m^2/g. Therefore, it is clear that the surface area plays a limited role in the gas sensing performance of these particular sensors.

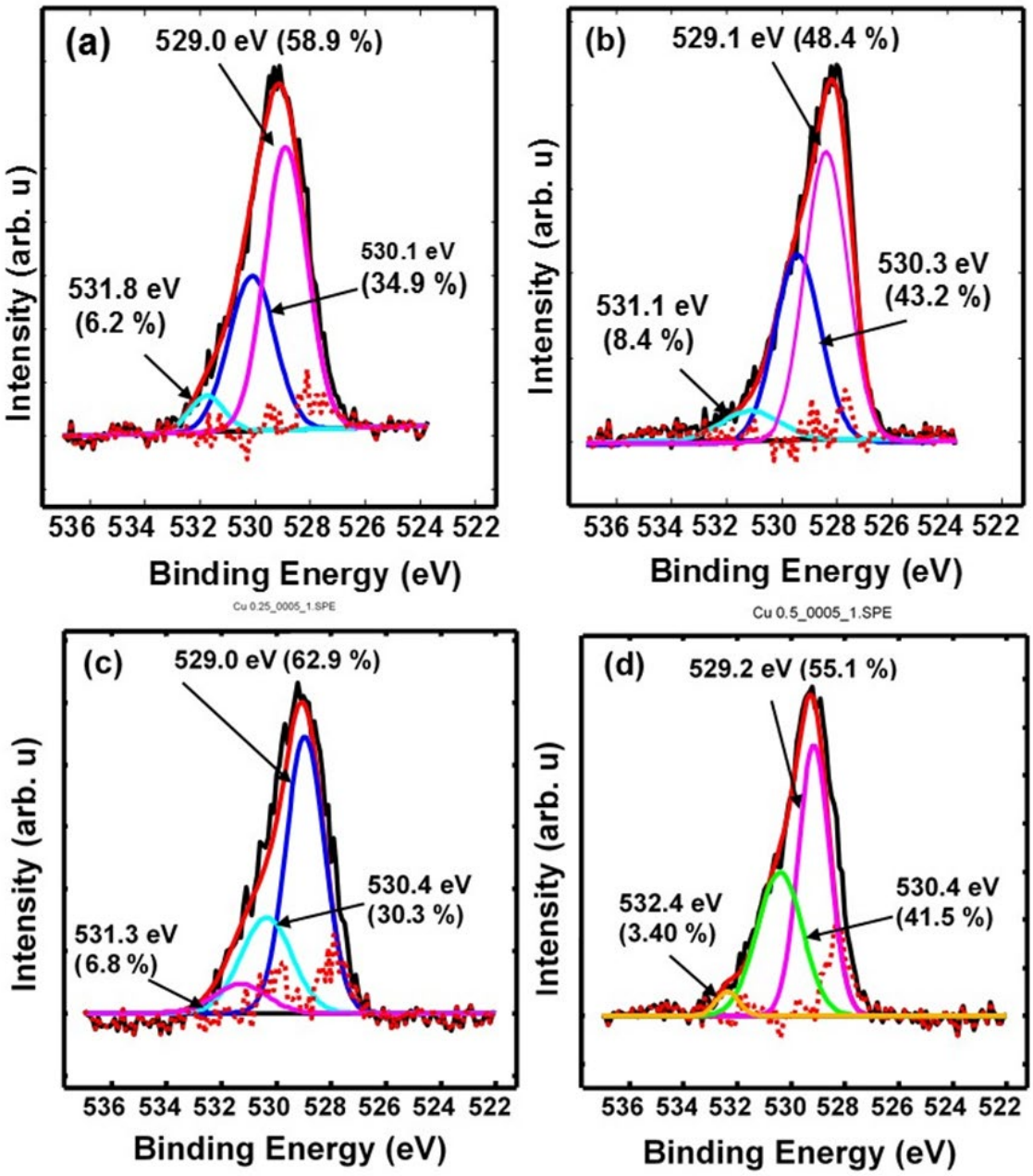

Figure 4. 8. *The O 1s XPS spectra of (a) pure CuO, (b) 0.1, (c) 0.25 and (d) 0.5 at. % Zn doped CuO nanoplatelets.*

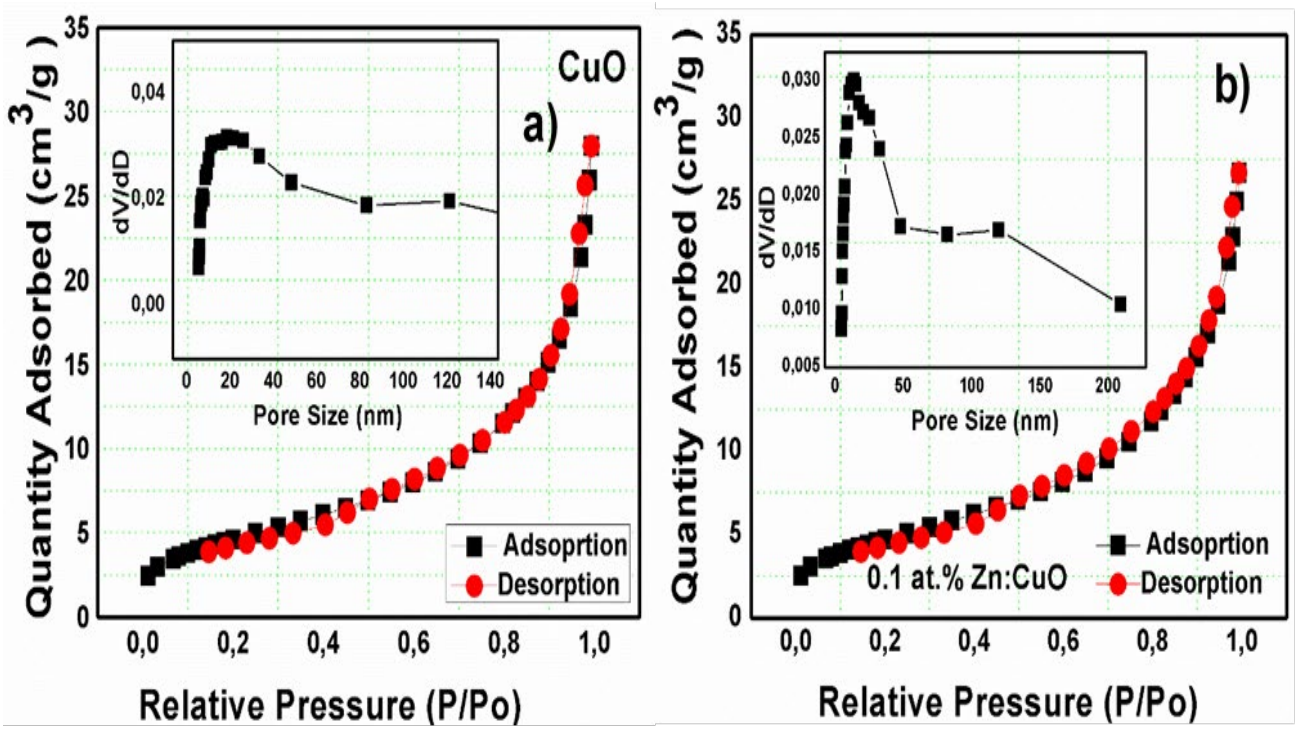

Figure 4. 9. *N2 adsorption-desorption isotherms of (a) pure CuO and (b) Zn doped CuO with various concentrations of Zn. insets show the corresponding pore sizes distributions.*

4.7. Magnetic Properties of Zn doped CuO and undoped CuO nanostructures

Since it is known that ferromagnetism at room temperature can also be driven by point defects **[15-17]**, we carried out magnetization measurements using a VSM in order to validate any putative relationship to sensing properties observed in pure CuO and Zn-doped CuO nanoplatelets. Figure 4.10 shows the magnetic field dependence of the magnetization of the sensor materials measured at room temperature up to a magnetic field strength of 14 kOe. The Magnetic parameters extracted such as saturation magnetization (M_S), coercivity (H_C) and squareness ratio (M_R/M_S) are presented in **Table 4.1**. It is clear from the Figure 10 that the samples demonstrated characteristics

of paramagnetic (PM) features at room temperature with low coercive fields. Moreover, the coercive field decreased with increasing Zn doping concentration, whereas the retentivity increased. The 0.1 at. % Zn doped sample exhibited higher M_S compared to its counterparts. Lu *et al*. **[16]** and Wang *et al*. **[17]** have also reported on composites systems of ZnO-CuO and their magnetic properties.

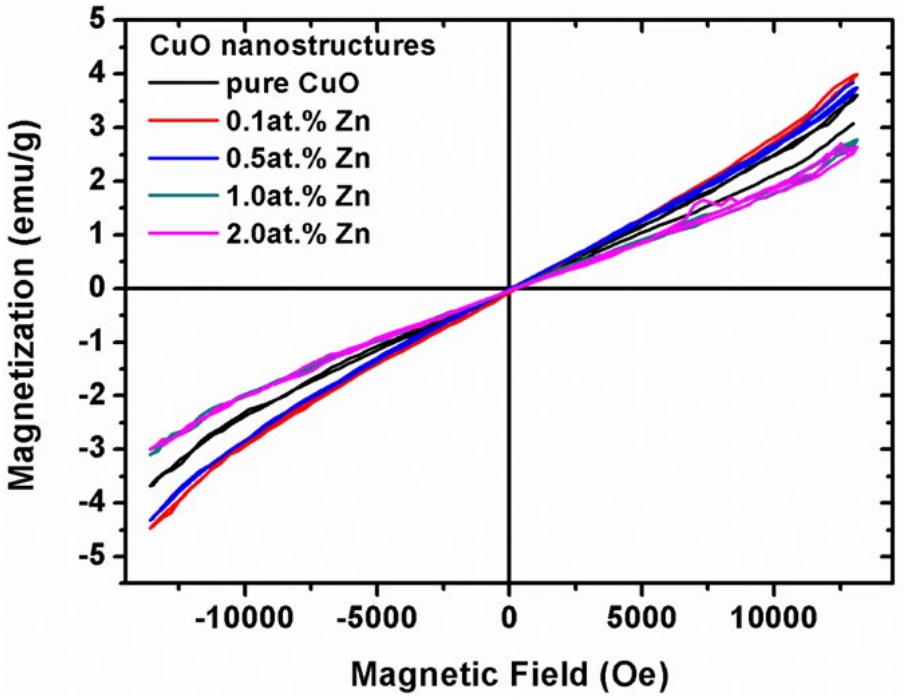

Figure 4. 10. *The Room Temperature Magnetization curves pure CuO and Zn doped CuO at different atomic concentration.*

***Table 4. 1**. Coercive field, saturation magnetization, squareness ratio for the hydrothermally grown pure CuO and Zn-doped CuO nanoplatelets.*

Samples *x*:CuO	**H_{ci} (Oe) ± 3**	**M_s (emu/g) ± 0.2**	**M_R/M_s ±0.003**
CuO	47.5	3.61	3.9×10^{-3}
0.1 at.%	40.4	4.23	3.3×10^{-3}
0.5 at.%	43.0	4.08	3.1×10^{-3}
1.0 at.%	1.6	2.94	652×10^{-3}
2.0 at.%	2.1	2.85	615×10^{-3}

These authors argued that once the composites ratios exceeded 50% of CuO, the paramagnetic feature dominates and the ferromagnetic part is weakened. It should be noted that Cu solid solubility is low or poor to ZnO **[18]**. However, CuO is well known to possess intrinsic paramagnetism **[20, 21]**. Therefore, the observed pure intrinsic paramagnetic signal is clear evidence of issues of solid solubility, lack of oxygen vacancies and the nature of CuO magnetization. This suggests that the observed paramagnetic nature of these sensors is evident to a small vestige of defects related to oxygen vacancies. This magnetization measurement is well supported by the PL and XPS analyses discussed above.

References

[1]. Ioannis Kortidis, Hendrik C. Swart, Suprakas Sinha Ray, David, E. Motaung. *Detailed understanding on the relation of various pH and synthesis reaction times towards a prominent low temperature H_2S gas sensor based on ZnO nanoplatelets.* Results in Physics 12, 2189-2201, (2019).

[2]. G.K. Williamson, W.H. Hall. *X-ray line broadening from filed aluminium and wolfram*. Acta Metall, 1, 22-31, (1953).

[3]. B. Kim, J.-H. Ahn, J. Y., C.-S. Lee, Y. C. Kang, F. Abdel-Hady, A. A. Wazzan, and J.-H. Lee. *Highly Selective Xylene Sensor Based on NiO/$NiMoO_4$ Nanocomposite Hierarchical Spheres for Indoor Air Monitoring*. ACS Applied Materials. Interfaces 50, 34603-34611, (2016).

[4]. N. Zhang, S. Ruan, J. Han, Y. Yin, X. Li, C. Liu, S. Adimi, S. Wen, Y. Xu, *Oxygen vacancies dominated CuO@$ZnFe_2O_4$ yolk-shell microspheres for robust and selective detection of xylene,* Sensors and Actuators: B 295, 117-126, (2019).

[5]. B. Zhang, F. Qu, X. Zhou, S. Zhang, T. Thomas, M. Yang. *Porous coral-like $NiCo_2O_4$ nanospheres with promising xylene gas sensing properties.* Sensors & Actuators B 261, 203-209, (2018).

[6]. J.-H. Kim, H.-M. Jeong, C.W. Na, J.-W. Yoon, F. Abdel-Hady, A.A. Wazzan, J.-H. Lee. *Highly selective and sensitive xylene sensors using Cr_2O_3-$ZnCr_2O_4$ hetero-nanostructures prepared by galvanic replacement.* Sensors & Actuators B 235, 498-506, (2016).

[7]. I. Kortidis, S. Lushozi, N. Leshabane, S. S. Nkosi, O. M. Ndwandwe, J. Tshilongo, N. Ntsasa, D. E. Motaung. *Selective detection of propanol vapour at low operating temperature utilizing ZnO nanostructures*. Ceramics International 45, 16417-16423, (2019).

[8]. I. Kortidis, H.C. Swart, S. Sinha Ray, D.E. Motaung, *Characteristics of point defects on the room temperature ferromagnetic and highly NO_2 selectivity gas sensing of p-type Mn_3O_4 nanorods,* Sensors and Actuators B: Chemical, 285, 92-107, (2019).

[9]. M.E. Franke, T.J. Koplin, U. Simon. *Metal and metal oxide nanoparticles in chemi-resistors: does the nanoscale matter*. Small 2, 36–50, (2006).

[10]. Jae-Hun Kim, Jae-Hyoung Lee, Yujung Park, Jin-Young Kim, Ali Mirzaei, Hyoun Woo Kimb, Sang Sub Kim. *Toluene- and benzene-selective gas sensors based on Pt- and Pd-functionalized ZnO nanowires in self-heating mode.* Sensors & Actuators: B. Chemical 294, 78-88, (2019).

[11]. Bo-Young Kim, Ji-Wook Yoon, Jin Koo Kim, Yun Chan Kang, Jong-Heun Lee. *Dual Role of Multiroom-Structured Sn-Doped NiO Microspheres for Ultrasensitive and Highly Selective Detection of Xylene.* ACS Applied Material. Interfaces 10, 16605-16612, (2018).

[12]. L. Zhang, L. Yin, C. Wang, N. Lun, Y. Qi and D. Xiang. *Origin of Visible Photoluminescence of ZnO Quantum Dots: Defect-Dependent and Size-Dependent*. J. Physical Chemistry. C 114, 9651–9658, (2010).

[13]. Wooseok Kim, Mingi Choi, Kijung Yong. *Generation of oxygen vacancies in ZnO nanorods/films and their effects on gas sensing properties*. Sens. Actuators B 209, 989-996, (2015).

[14]. Sanjit Sarkar, Durga Basak. *Synthesis of dense intersecting branched tree-like ZnO nanostructures and its superior LPG sensing property.* Sens. Actuators B 176, 374-378, (2013).

[15]. Prakash Chand Anurag Gaur Ashavani Kumar Umesh Kumar Gaur. *Structural and optical study of Li doped CuO thin films on Si (1 0 0) substrate deposited by pulsed laser deposition.* Applied Surface Science 15, 280-286, (2014).

[16]. X. Zhao, P. Wang, Z. Yan, N. Ren. *Room temperature photoluminescence properties of CuO nanowire arrays*. Optical Materials. 42, 544-547, (2015).

[17]. Ping Lu, Wei Zhou, Ying Li, Jianchun Wang, Ping Wu. *CuO nanosheets/ZnO nanorods synthesized by a template-free hydrothermal approach and their optical and magnetic characteristics.* Ceramics International 43, 9798–9805, (2017).

[18]. Lukas Mai, Felix Mitschker, Claudia Bock, Alessia Niesen, Engin Ciftyurek, Detlef Rogalla, Johannes Mickler, Matthias Erig, Zheshen Li, Peter Awakowicz, Klaus Schierbaum, Anjana Devi. *From Precursor Chemistry to Gas Sensors: Plasma-Enhanced Atomic Layer Deposition Process Engineering for Zinc Oxide Layers from a Nonpyrophoric Zinc Precursor for Gas Barrier and Sensor Applications*. Small 1907506 1-12. DOI: 10.1002/smll.201907506, (2020).

[19]. Wen Wang, Linhua Xu, Ruofan Zhang, Jilin Xu, Fenglin Xian, Jing Su, Fan Yang. *Coexistence of ferromagnetism and paramagnetism in ZnO/CuO nanocomposites*. Chemical Physics Letters 721, 57-61, (2019).

[20]. David E Motaung, Gugu H Mhlongo, Steven S Nkosi, Gerald F Malgas, Bonex W Mwakikunga, E. Coetsee, Hendrik C Swart, H. M. I. Abdallah, Thomas Moyo, Suprakas S Ray. *Shape-Selective Dependence of Room Temperature Ferromagnetism Induced by Hierarchical ZnO Nanostructures.* ACS Applied Materials. Interfaces 6, 8981-8995, (2014).

[21]. N. Abrahama, A. Rufus, C. Unni, D. Philip. *Dye sensitized solar cells using catalytically active CuO-ZnO nanocomposite synthesized by single step method.* Spectrochim. Acta Part A 200, 116–126, (2018).

CHAPTER V

5.1. Cconclusions and Recommendations

In summary, pure and Zn doped CuO nanoplatelets were successfully synthesized by a facile pressurized hydrothermal chemical process. Pure CuO matrix was doped with Zn at various atomic concentrations (0.1, 0.25, 0.5, 1.0 and 2.0 at. %). The undoped CuO and 0.1 at. % Zn doped CuO based sensors were subjected to nine different gases at various concentrations and activation temperatures. Amongst the sensors, pure CuO and 0.1 at. % Zn doped CuO proved to be the best sensor materials, showing resistance ratios of about 42 and 53 towards 100 ppm p-xylene gas at a low optimum operating temperature of 150 °C. The PL studies at room and elevated temperatures suggest that both sensors contained no or small traces of oxygen vacancies and/or oxygen interstitials. At 150 °C the 0.1 at. % Zn doped CuO emitted a broad visible luminescence which may be attributed to oxygen interstitials and vacancies (V_o). Meanwhile, the pure CuO PL emission at 150 °C was completely supressed. These two sensors (CuO and 0.1 at. % Zn doped CuO) demonstrated highly selective and sensitive to p-xylene target gas although XPS, PL, and VSM measurements suggested only vestiges of V_o defects.

The claims **[1-7]** that oxygen vacancies are responsible for the high responses gas sensing remain unclear as is demonstrated in this current work. The studies

demonstrate the synthesis and fabrication of CuO and Zn-doped CuO nanoplatelets at various atomic percentages showing no or small contents of oxygen vacancies and interstitials defects at room-temperature meanwhile at elevated temperatures these defects emerged except the pure CuO. Pure CuO and 0.1 at. % doped-Zn: CuO showed highly sensitive and selective behaviour with responses of 42 and 53, respectively. The electronic chemiresistive gas sensing hypothesis mechanism goes beyond the attributes of the intrinsic defects i.e. oxygen vacancies and their interstitials.

The future trend and perspective in the gas sensing should focus on the fundamental gas sensing mechanisms (electronic and ionic-activated conductivities) in different ambient conditions i.e. inert without/reduced oxygen and dry with oxygen, but low relative humidity. The gas detection and long-term monitoring are two crucial factors that form part of our future outlook. The simultaneous exposure, cross selectivity, also is one crucial factor within the gas sensing field. The better understanding of these factors will assist in designing of the portable, hand-held sensor device operating at low temperatures and possible a self-powered integrated sensor.

A high efficiency design, including high response, fast response time and fast recovery time is essential for low temperature gas sensors.

References

[1]. Wooseok Kim, Mingi Choi, Kijung Yong. *Generation of oxygen vacancies in ZnO nanorods/films and their effects on gas sensing properties.* Sens. Actuators B 209, 989-996, (2015).

[2]. Sanjit Sarkar, Durga Basak. *Synthesis of dense intersecting branched tree-like ZnO nanostructures and its superior LPG sensing property*. Sens. Actuators B 176, 374-378, (2013).

[3]. M. –W. Ahn, K.-S. Park, J.-H. Heo, J.-G. Park, D.-W. Kim, K.J. Choi, J.-H. Lee, S.-H. Hong. *Gas sensing properties of defect-controlled ZnO-nanowire gas sensor*. Appl. Phys. Lett. 93, 263103 (2008).

[4]. Sumati Pati, S.B. Majumder, P. Banerji. *Role of oxygen vacancy in optical and gas sensing characteristics of ZnO thin films.* J. Alloys & Compounds 541, 376-379, (2012).

[5]. Nguyen Duc Khoang, *Do Dang Trung, Nguyen Van Duy, Nguyen Duc Hoa, Nguyen Van Hieu. Design of SnO_2/ZnO hierarchical nanostructures for enhanced ethanol gas-sensing performance.* Sensors and Actuators B 174, 594-601, (2012).

[6]. Chao Zhang, Xin Geng, Jiawei Li, Yifan Luo, Pengfei Lu. *Role of oxygen vacancy in tuning of optical, electrical and NO_2 sensing properties of ZnO_{1-x} coatings at room temperature*. Sensors and Actuators B 248, 886-893, (2017).

[7]. S.S. Nkosi, I. Kortidis, D.E. Motaung, R.E. Kroon, N. Leshabane, J. Tshilongo, O.M. Ndwandwe. *The effect of stabilized ZnO nanostructures green luminescence towards LPG sensing capabilities.* Materials Chemistry and Physics 242, 122452, (2020).

Appendix A - Section

Supplementary Information (ESI):

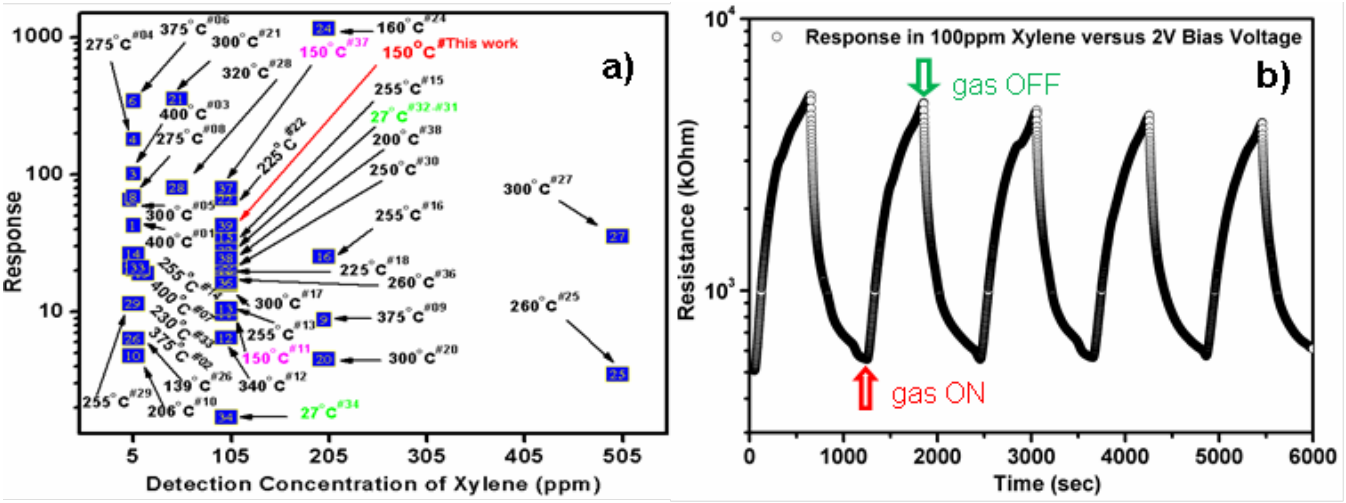

Figure. S1. *(a) Comparison literature survey plot for all the sensors dedicated to p-Fig. xylene gas detection and their operating temperatures* ***[1-38]****. (b) Repeatability cycles for the 2 V bias over 100 ppm xylene gas at 150 °C.*

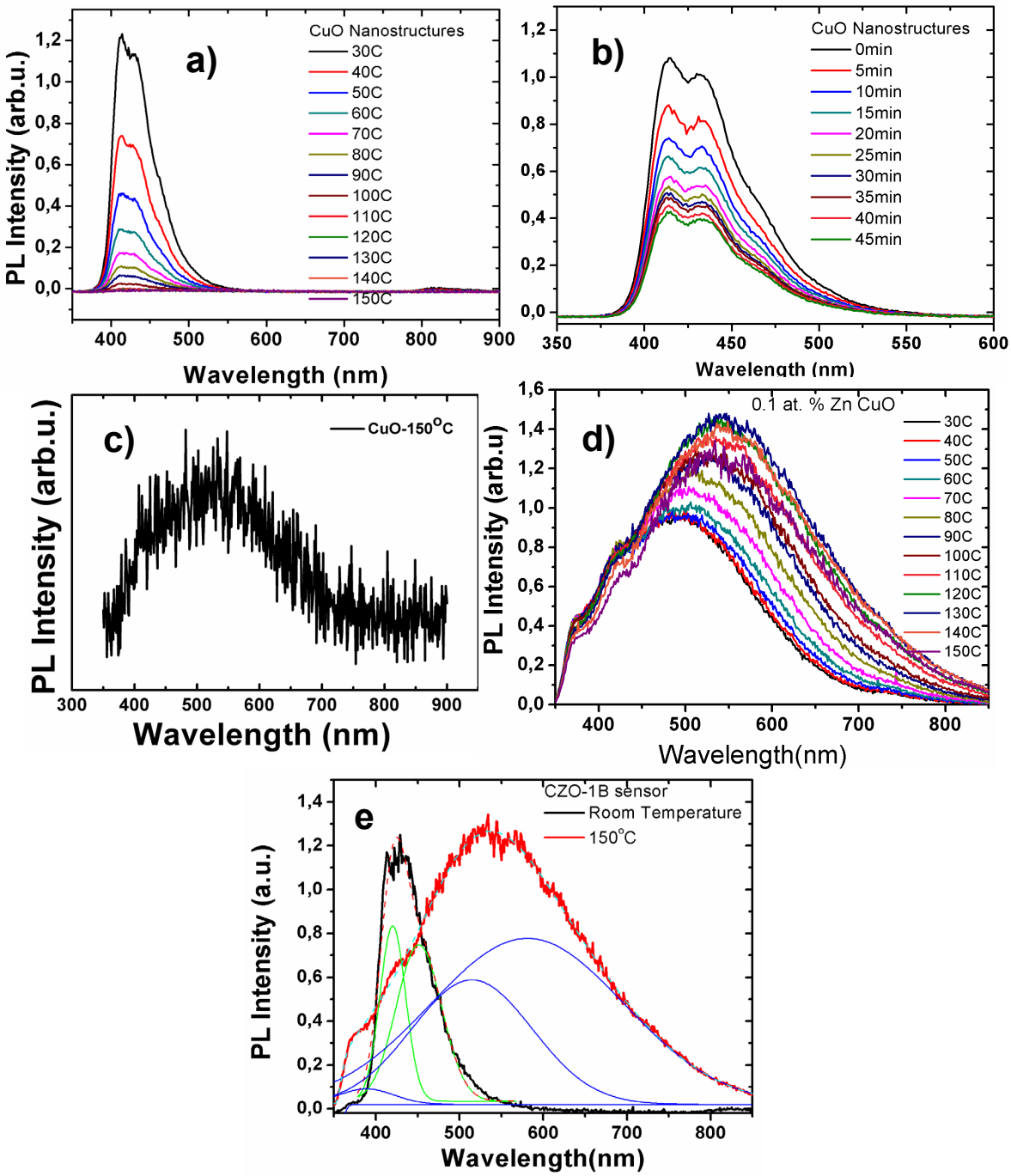

Figure. S2. *Photoluminescence spectra of the pure CuO and 0.1 at. % Zn-doped CuO (CZO-1B) time stability and temperature dependence.*

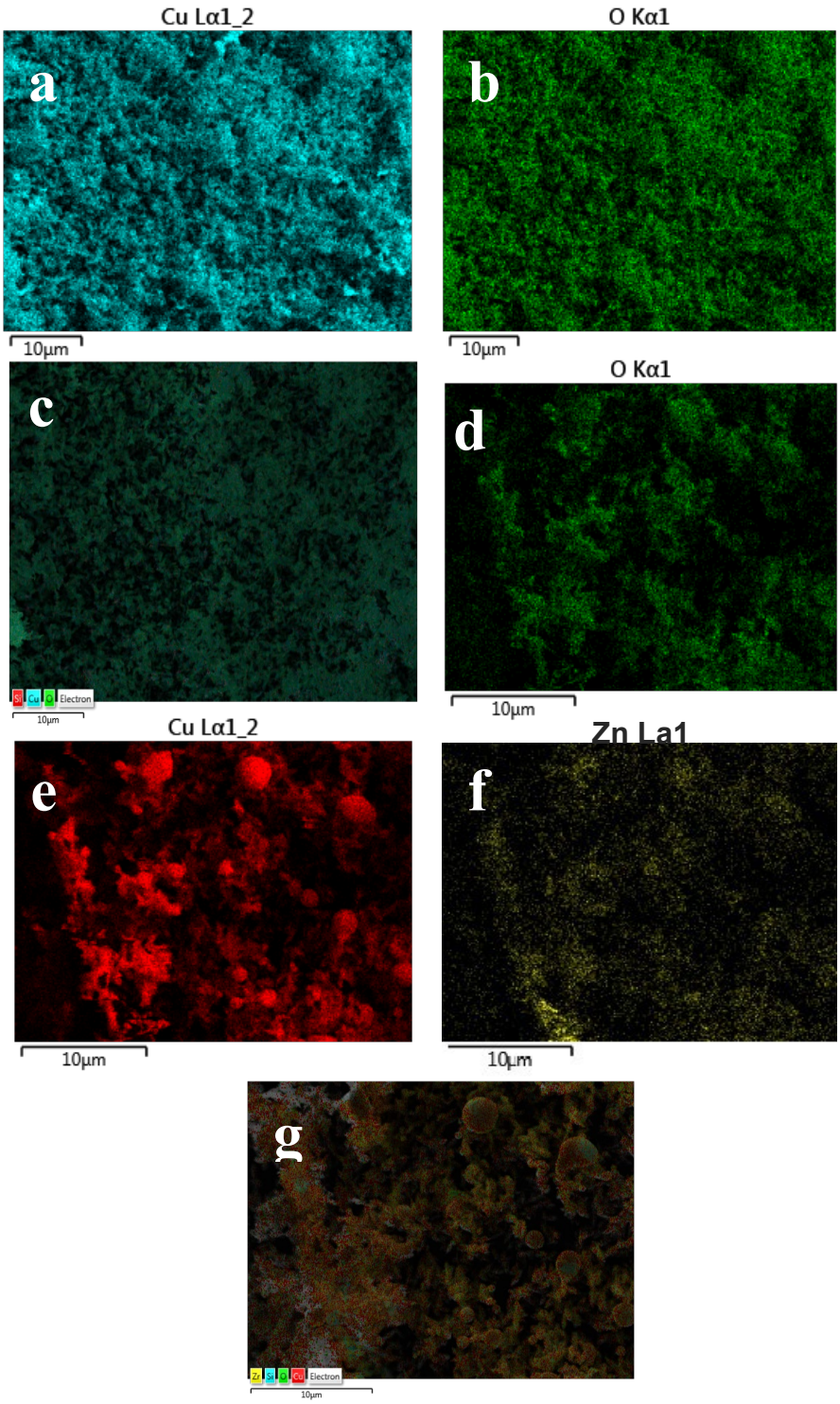
Cu Lα1_2
a
10μm
O Kα1
b
10μm
c
Electron
10μm
O Kα1
d
10μm
Cu Lα1_2
e
10μm
Zn La1
f
10μm
g
Electron
10μm

Figure. S3. *SEM micrographs elemental mapping for both the pure CuO (a-c) and 0.1 at.% Zn-doped CuO (d-g). Both (c) and (f) correspond to the combined elemental mapping of Cu, O, and Cu, O, 0.1 at. % Zn, respectively.*

The following figures correspond to the XPS spectral surveys, Cu 2p and O 1s analysis for all the samples, CuO and Zn-doped CuO at various atomic percentages.

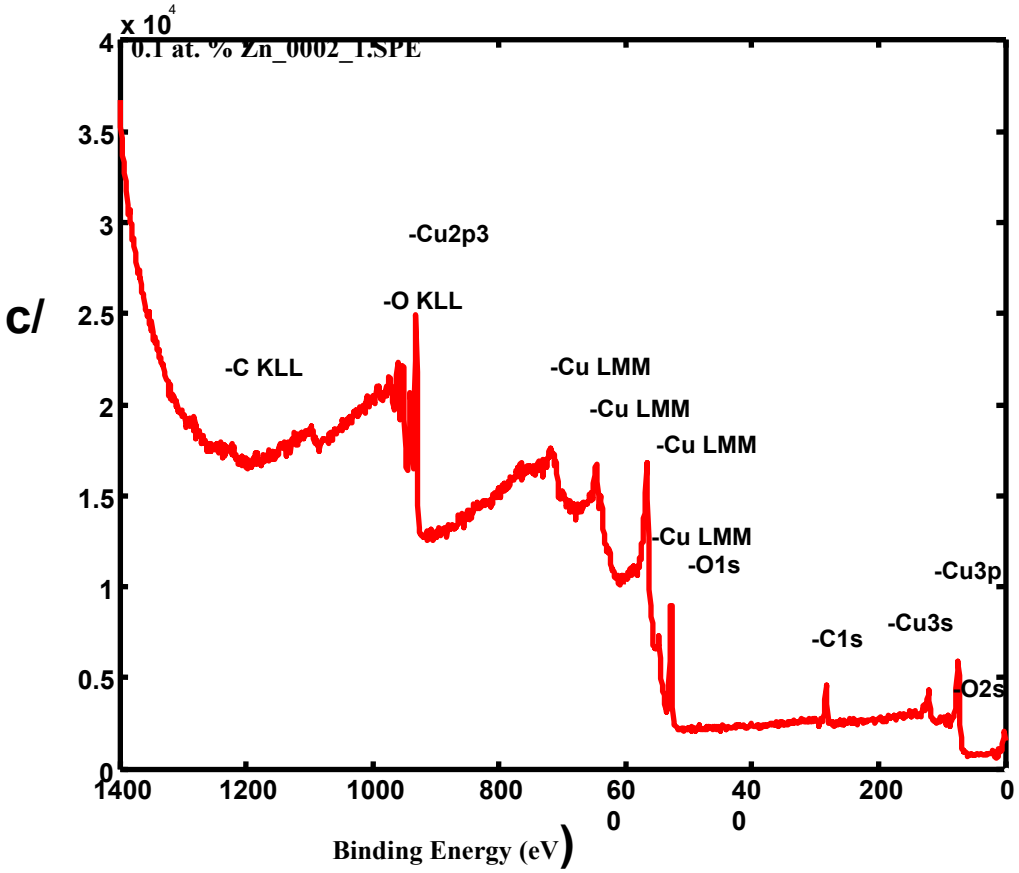

Figure. S4. *XPS survey spectrum for the 0.1 at. % Zn-doped CuO nanoplatelets.*

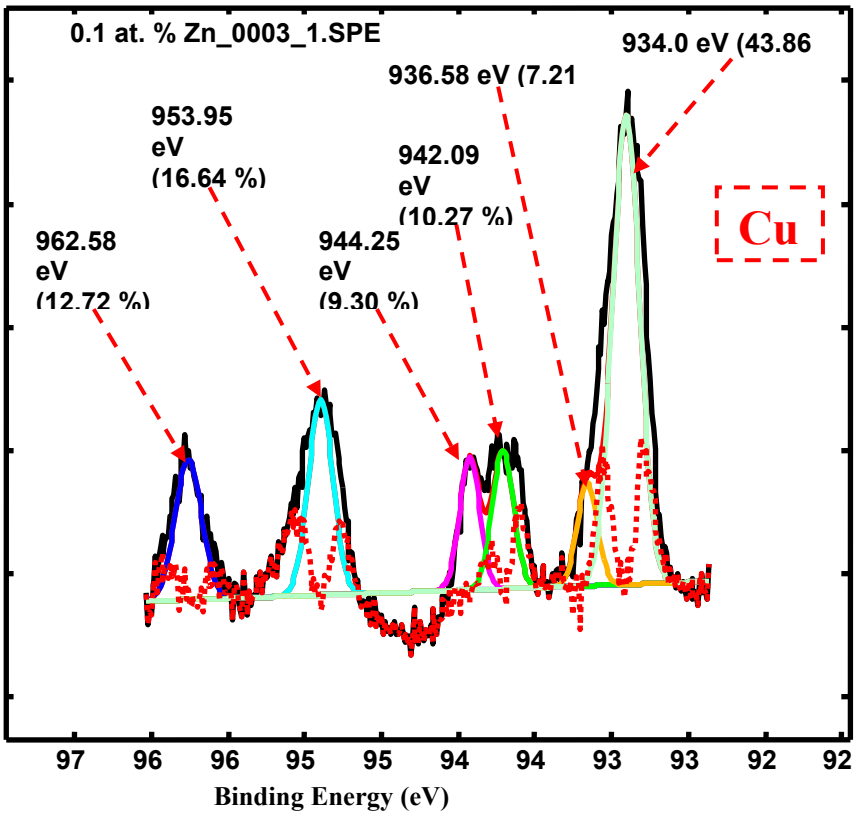

Figure. S5. *Showing the binding energies from the XPS survey spectrum for the 0.1 at. % Zn-doped CuO nanoplatelets.*

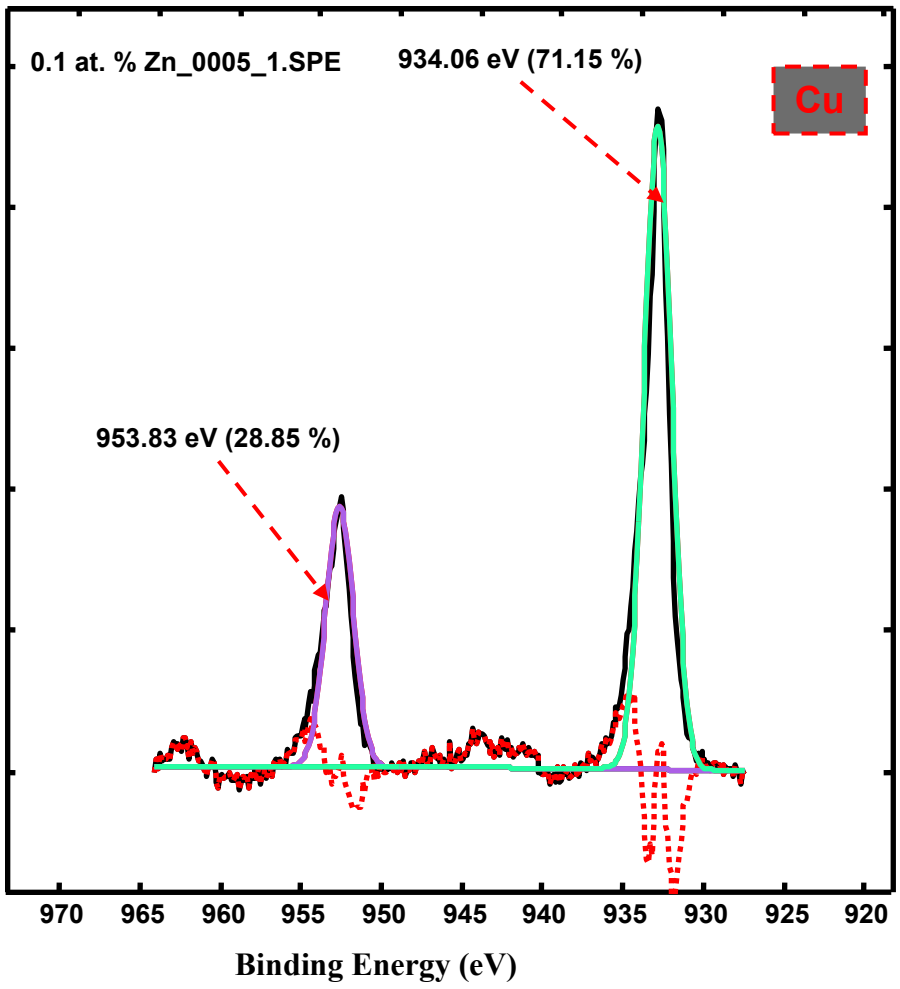

Figure. S6. *Showing the binding energies of Cu from the XPS survey spectrum for the 0.1 at. % Zn-doped CuO nanoplatelets.*

Reference

1. H.-S. Woo, C.-H. Kwak, J.-H. Chung, J.-H. Lee, *Highly selective and sensitive xylene sensors using Ni-doped branched ZnO nanowire networks*, Sen. Actuators, B: Chem. 216, 358–366 (2015).

2. H.-S. Woo, C.-H. Kwak, J.-H. Chung, J.-H. Lee, *Co-Doped Branched ZnO Nanowires for Ultra-selective and Sensitive Detection of Xylene*, ACS Appl. Mater. Interfaces, 6, 22553-22560 (2014).

3. B.-Y. Kim, J.-H. Ahn, J.-W. Yoon, C.-S. Lee, Y.C. Kang, F.A. Hady, A.A. Wazzan, J.-H. Lee, *Highly selective xylene sensor based on NiO/$NiMoO_4$ nanocomposite hierarchical spheres for indoor air monitoring*, ACS Appl. Mater. Interfaces, 8, 34603-34611 (2016).

4. S.-J. Hwang, K.-L. Choi, J.-W. Yoon, Y.C. Kang, J.-H. Lee, *Pure and Palladium-Loaded Co_3O_4 Hollow Hierarchical Nanostructures with Giant and Ultra-selective Chemiresistivity to Xylene and Toluene*, Chem. Eur. J. 21, 5872 – 5878 (2015).

5. T.-H. Kim, C.-H. Kwak, J.-H. Lee, *NiO/$NiWO_4$ Composite Yolk-Shell Spheres with Nano-Scale NiO Outer Layer for Ultrasensitive and Selective Detection of Sub-ppm-level p-Xylene*, Appl. Mater. Interfaces 9, 32034-32043 (2017).

6. H.-J. Kim, J.-W Yoon, K.-I. Choi, H.W. Jang, A. Umar, J.-H. Lee, *Ultra-selective and sensitive detection of xylene and toluene for monitoring indoor air pollution using Cr-doped NiO hierarchical nanostructures,* Nanoscale, 5, 7066 (2013).

7. J.-H. Kim, H.-M. Jeong, C.W. Na, J.-W. Yoon, F.A. Hady, A.A. Wazzan, J.-H. Lee, *Highly selective and sensitive xylene sensors using Cr_2O_3-$ZnCr_2O_4$ hetero-nanostructures prepared by galvanic replacement,* Sen. Actuators, B: Chem. 235, 498–506 (2016).

8. C. Feng, C. Wang, H. Zhang, X. Li, C. Wang, P. Cheng, J. Ma, P. Sun, Y. Gao, H. Zhang, Y. Sun, J. Zheng, G. Lu, *Enhanced sensitive and selective xylene sensors using W-doped NiO nanotubes,* Sen. Actuators, B: Chem. 221, 1475–1482 (2015).

9. D. Jiang, W. Wei, F. Li, Y. Li, C. Liu, D. Sun, C. Feng, S. Ruan, *Xylene gas sensor based on a-MoO_3/a-Fe_2O_3 heterostructure with high response and low operating temperature*, RSC Adv., 5, 39442- 39448, (2015).

10. Y. Cao, P. Hu, W. Pan, Y. Huang, D. Jia, *Methanal and xylene sensors based on ZnO nanoparticles and nanorods prepared by room-temperature solid-state chemical reaction*, Sen. Actuators, B: Chem. 134, 462–466, (2008).

11. Y. Li, Y. Cao, D. Jia, Y. Wang, J. Xie, *Solid-state chemical synthesis of mesoporous-Fe_2O_3 nanostructures with enhanced xylene-sensing properties*, Sen. Actuators, B: Chem. 198, 360-365, (2014).

12. F. Qu, C. Feng, C. Li, W. Li, S. Ruan, S. Wen, H. Zhang, *Preparation and Xylene-Sensing Properties of Co_3O_4 Nanofibers*, Int. J. Appl. Ceram. Technol., 11, 619–625, (2014).

13. F. Li, S. Guo, J. Shen, L. Shen, D. Sun, B. Wang, Y. Chen, S. Ruan, *Xylene gas sensor based on Au-loaded $WO_3 \cdot H_2O$ nanocubes with enhanced sensing performance*, Sen. Actuators, B: Chem. 238, 364–373, (2017).

14. F. Li, S. Ruana, N. Zhang, Y. Yin, S. Guo, Yu Chena, H. Zhang, C. Li, *Synthesis and characterization of Cr-doped WO_3 nanofibers for conductometric sensors with high xylene sensitivity*, Sen. Actuators, B: Chem. 265, 355–364, (2018).

15. H. Gao, Q. Yu, S. Zhang, T. Wang, P. Sun, H. Lu, F. Liu, X. Yan, F. Liu, X. Liang, Y. Gao, G. Lu, *Nanosheet-assembled NiO microspheres modified by Sn^{2+} ions isovalent interstitial doping for xylene gas sensors,* Sen. Actuators, B: Chem. 269, 210–222, (2018).

16. K. Xu, Y. Yang, T. Yu, C. Yuan, *WO_3 nanofibers anchored by porous $NiCo_2O_4$ nanosheets for xylene detection,* Ceram. Int. 44, 21717–21724, (2018).

17. H. Gao, D. Wei, P. Lin, C. Liu, P. Sun, K. Shimanoe, N. Yamazoe, G. Lu, *The design of excellent xylene gas sensor using Sn-doped NiO hierarchical nanostructure,* Sen. Actuators, B: Chem. 253, 1152–1162, (2017).

18. G. Khorshidi, M. Behzad, H.S. Jahromi, E. Alaie, *Influence of metal (W, Pd)-doping on gas sensing properties of the NiO flower-like thin films for o-xylene detection,* J. Alloys Compd. 737, 122-129, (2018).

19. C. Feng, X. Kou, B. Chen, G. Qian, Y. Sun, G. Lu, *One-pot synthesis of In doped NiO nanofibers and their gassensing properties,* Sen. Actuators, B: Chem. 253, 584–591, (2017).

20. H. Gao, Q. Yu, K. Chen, P. Sun, F. Liu, X. Yan, F. Liu, G. Lu, *Ultrasensitive gas sensor based on hollow tungsten trioxide-nickel oxide (WO_3-NiO) nano-flowers for fast and selective xylene detection*, J. Colloid Interface Sci. 535, 458–468, (2019).

21. H. Gao, J. Guo, Y. Li, C. Xie, X. Li, L. Liu, Y. Chen, P. Sun, F. Liu, X. Yan, F. Liu, G. Lu, *Highly selective and sensitive xylene gas sensor fabricated from NiO/$NiCr_2O_4$ p-p nanoparticles*, Sen. Actuators, B: Chem. 284, 305–315, (2019).

22. J. Cao, Z. Wang, R. Wang, T. Zhang, *Electrostatic sprayed Cr-loaded NiO core-in hollow-shell structured micro/nanospheres with ultra-selectivity and sensitivity for xylene,* Cryst. Eng. Comm, 16, 7731-7737, (2014).

23. N. Chen, D. Deng, Y. Li, X. Xing, X. Liu, X. Xiao and Y. Wang, *Xylene sensing performance of WO_3 decorated anatase TiO_2 nanoparticles as a sensing material for gas sensor at low operating temperature*, RSC Adv. 6, 49692-49701, (2016).

24. C. Yang, F. Xiao, J. Wang, X. Su, *3D flower- and 2D sheet-like CuO nanostructures: Microwave-assisted synthesis and application in gas sensors,* Sen. Actuators, B: Chem. B 207, 177–185, (2015).

25. Y. Li, X Ma, S Guo, B Wang, D. Sun, X. Zhang, S. Ruan, *Hydrothermal synthesis and enhanced xylene sensing properties of pompon-like Cr-doped Co_3O_4 hierarchical nanostructures*, RSC Adv., 6, 22889-22895, (2016).

26. Y. Zhang, Y. Zhou, Z. Li, G. Chen, Y. Mao, H. Guan, C. Dong, *MOFs-derived $NiFe_2O_4$ fusiformis with highly selective response to xylene,* J. Alloys Compd 784, 102-110, (2019).

27. L. Deng, X. Ding, D. Zeng, S. Zhang, C. Xie, *High Sensitivity and Selectivity of C-Doped WO_3 Gas Sensors Toward Toluene and Xylene,* IEEE SENSORS J., 12, 2209-2214, (2012).

28. F. Qu, W. Shan, D. Wang, S. Du, T. Thomas, S. Ruan, M. Yang, *Coordination Polymers Derived Multi-shells Mixed Ni-Co Oxides Microspheres for Robust and Selective Detection of Xylene*, ACS Appl. Mater. Interfaces, 10, 15314-15321, (2018).

29. L.-L. Sui, X.-F. Zhang, X. Cheng, P. Wang, Y.-M. Xu, S. Gao, H. Zhao, L.-H. Huo, *Au-loaded hierarchical MoO3 hollow spheres with enhanced gas sensing performance for the detection of BTX (benzene, toluene and xylene) and the sensing mechanism*, ACS Appl. Mater. Interfaces, 9, 1661-1670, (2017).

30. Y. Vijayakumar, G.K. Mani, D. Ponnusamy, P. Shankar, A.J. Kulandaisamy, K. Tsuchiya, J.B B. Rayappan, M.V.R. Reddy, *V_2O_5 nanofibers: Potential contestant for high performance xylene sensor,* J. Alloys Compd. 731, 805-812, (2018).

31. Y. Vijayakumara, G.K. Mani, M.V.R. Reddy, J.B.B. Rayappan, *Nanostructured flower like V_2O_5 thin films and its room temperature sensing characteristics,* Ceram. Int. 41, 2221–2227, (2015).

32. F. Lia, Q. Qina, N. Zhanga, C. Chenc, L. Sunc, X. Liuc, Y. Chena, C. Li, S. Ruan, *Improved gas sensing performance with Pd-doped $WO_3 \cdot H_2O$ nanomaterials for the detection of xylene*, Sen. Actuators, B: Chem. 244 837–848, (2017).

33. D.K. Subbiah, A.J. Kulandaisamy, R.B. George, P. Shankar, G.K. Mani, K.J. Babu, J.B.B. Rayappan, *Nano ceria as xylene sensor - Role of cerium precursor*, J. Alloys Compd 753 771-780, (2018).

Publication

- **Ongezwa Mnethu**, Steven S. Nkosi*, Ioannis Kortidis, David E. Motaung, R.E. Kroon, Hendrik C. Swart, Napo G. Ntsasa, James Tshilongo, Thomas Moyo. ***Ultra-Sensitive and Selective p-xylene Gas Sensor at Low Operating Temperature Utilizing Zn doped CuO Nanoplatelets: Insignificant Vestiges of Oxygen Vacancies***. Journal of Colloids and Interface Science 576 (2020) 364 – 375. **IF 8.128**